Available on CMS information server

CMS NOTE -2009/002

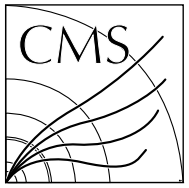

The Compact Muon Solenoid Experiment

CMS Note

Mailing address: CMS CERN, CH-1211 GENEVA 23, Switzerland

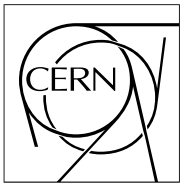

06 June 2008 (v6, 08 December 2008)

CMS Tracker Alignment at the Integration Facility

W. Adam, T. Bergauer, M. Dragicevic, M. Friedl, R. Frühwirth, S. Hänsel, J. Hrubec, M. Krammer, M.Oberegger, M. Pernicka, S. Schmid, R. Stark, H. Steininger, D. Uhl, W. Waltenberger, E. Widl

Institut für Hochenergiephysik der Österreichischen Akademie der Wissenschaften (HEPHY), Vienna, Austria

P. Van Mechelen, M. Cardaci, W. Beaumont, E. de Langhe, E. A. de Wolf, E. Delmeire, M. Hashemi

Universiteit Antwerpen, Belgium

O. Bouhali, O. Charaf, B. Clerbaux, J.-P. Dewulf. S. Elgammal, G. Hammad, G. de Lentdecker, P. Marage, C. Vander Velde, P. Vanlaer, J. Wickens

Université Libre de Bruxelles, ULB, Bruxelles, Belgium

V. Adler, O. Devroede, S. De Weirdt, J. D'Hondt, R. Goorens, J. Heyninck, J. Maes, M. Mozer, S. Tavernier, L. Van Lancker, P. Van Mulders, I. Villella, C. Wastiels

Vrije Universiteit Brussel, VUB, Brussel, Belgium

J.-L. Bonnet, G. Bruno, B. De Callatay, B. Florins, A. Giammanco, G. Gregoire, Th. Keutgen, D. Kcira, V. Lemaitre, D. Michotte, O. Militaru, K. Piotrzkowski, L. Quertermont, V. Roberfroid, X. Rouby, D. Teyssier

Université catholique de Louvain, UCL, Louvain-la-Neuve, Belgium

E. Daubie

Université de Mons-Hainaut, Mons, Belgium

E. Anttila, S. Czellar, P. Engström, J. Härkönen, V. Karimäki, J. Kostesmaa, A. Kuronen, T. Lampén, T. Lindén, P. -R. Luukka, T. Mäenpää, S. Michal, E. Tuominen, J. Tuominiemi

Helsinki Institute of Physics, Helsinki, Finland

M. Ageron, G. Baulieu, A. Bonnevaux, G. Boudoul, E. Chabanat, E. Chabert, R. Chierici, D. Contardo, R. Della Negra, T. Dupasquier, G. Gelin, N. Giraud, G. Guillot, N. Estre, R. Haroutunian, N. Lumb, S. Perries, F. Schirra, B. Trocme, S. Vanzetto

Université de Lyon, Université Claude Bernard Lyon 1, CNRS/IN2P3, Institut de Physique Nucléaire de Lyon, France

J.-L. Agram, R. Blaes, F. Drouhin[a)], J.-P. Ernenwein, J.-C. Fontaine

Groupe de Recherches en Physique des Hautes Energies, Université de Haute Alsace, Mulhouse, France

J.-D. Berst, J.-M. Brom, F. Didierjean, U. Goerlach, P. Graehling, L. Gross, J. Hosselet, P. Juillot, A. Lounis, C. Maazouzi, C. Olivetto, R. Strub, P. Van Hove

Institut Pluridisciplinaire Hubert Curien, Université Louis Pasteur Strasbourg, IN2P3-CNRS, France

G. Anagnostou, R. Brauer, H. Esser, L. Feld, W. Karpinski, K. Klein, C. Kukulies, J. Olzem, A. Ostapchuk, D. Pandoulas, G. Pierschel, F. Raupach, S. Schael, G. Schwering, D. Sprenger, M. Thomas, M. Weber, B. Wittmer, M. Wlochal

I. Physikalisches Institut, RWTH Aachen University, Germany

F. Beissel, E. Bock, G. Flugge, C. Gillissen, T. Hermanns, D. Heydhausen, D. Jahn, G. Kaussen[b)], A. Linn, L. Perchalla, M. Poettgens, O. Pooth, A. Stahl, M. H. Zoeller

III. Physikalisches Institut, RWTH Aachen University, Germany

P. Buhmann, E. Butz, G. Flucke, R. Hamdorf, J. Hauk, R. Klanner, U. Pein, P. Schleper, G. Steinbrück

University of Hamburg, Institute for Experimental Physics, Hamburg, Germany

P. Blüm, W. De Boer, A. Dierlamm, G. Dirkes, M. Fahrer, M. Frey, A. Furgeri, F. Hartmann[a)], S. Heier, K.-H. Hoffmann, J. Kaminski, B. Ledermann, T. Liamsuwan, S. Müller, Th. Müller, F.-P. Schilling, H.-J. Simonis, P. Steck, V. Zhukov

Karlsruhe-IEKP, Germany

P. Cariola, G. De Robertis, R. Ferorelli, L. Fiore, M. Preda,[c)], G. Sala, L. Silvestris, P. Tempesta, G. Zito

INFN Bari, Italy

D. Creanza, N. De Filippis[d)], M. De Palma, D. Giordano, G. Maggi, N. Manna, S. My, G. Selvaggi

INFN and Dipartimento Interateneo di Fisica, Bari, Italy

S. Albergo, M. Chiorboli, S. Costa, M. Galanti, N. Giudice, N. Guardone, F. Noto, R. Potenza, M. A. Saizu[c)], V. Sparti, C. Sutera, A. Tricomi, C. Tuvè

INFN and University of Catania, Italy

M. Brianzi, C. Civinini, F. Maletta, F. Manolescu, M. Meschini, S. Paoletti, G. Sguazzoni

INFN Firenze, Italy

B. Broccolo, V. Ciulli, R. D'Alessandro. E. Focardi, S. Frosali, C. Genta, G. Landi, P. Lenzi, A. Macchiolo, N. Magini, G. Parrini, E. Scarlini

INFN and University of Firenze, Italy

G. Cerati

INFN and Università degli Studi di Milano-Bicocca, Italy

P. Azzi, N. Bacchetta[a)], A. Candelori, T. Dorigo, A. Kaminsky, S. Karaevski, V. Khomenkov[b)], S. Reznikov, M. Tessaro

INFN Padova, Italy

D. Bisello, M. De Mattia, P. Giubilato, M. Loreti, S. Mattiazzo, M. Nigro, A. Paccagnella, D. Pantano, N. Pozzobon, M. Tosi

INFN and University of Padova, Italy

G. M. Bilei[a)], B. Checcucci, L. Fanò, L. Servoli

INFN Perugia, Italy

F. Ambroglini, E. Babucci, D. Benedetti[e)], M. Biasini, B. Caponeri, R. Covarelli, M. Giorgi, P. Lariccia, G. Mantovani, M. Marcantonini, V. Postolache, A. Santocchia, D. Spiga

INFN and University of Perugia, Italy

G. Bagliesi , G. Balestri, L. Berretta, S. Bianucci, T. Boccali, F. Bosi, F. Bracci, R. Castaldi, M. Ceccanti, R. Cecchi, C. Cerri, A .S. Cucoanes, R. Dell'Orso, D .Dobur, S .Dutta, A. Giassi, S. Giusti, D. Kartashov, A. Kraan, T. Lomtadze, G. A. Lungu, G. Magazzù, P. Mammini, F. Mariani, G. Martinelli, A. Moggi, F. Palla, F. Palmonari, G. Petragnani, A. Profeti, F. Raffaelli, D. Rizzi, G. Sanguinetti, S. Sarkar, D. Sentenac, A. T. Serban, A. Slav, A. Soldani, P. Spagnolo, R. Tenchini, S. Tolaini, A. Venturi, P. G. Verdini[a)], M. Vos[f)], L. Zaccarelli

INFN Pisa, Italy

C. Avanzini, A. Basti, L. Benucci[g)], A. Bocci, U. Cazzola, F. Fiori, S. Linari, M. Massa, A. Messineo, G. Segneri, G. Tonelli

University of Pisa and INFN Pisa, Italy

P. Azzurri, J. Bernardini, L. Borrello, F. Calzolari, L. Foà, S. Gennai, F. Ligabue, G. Petrucciani , A. Rizzi[h)], Z. Yang[i)]

Scuola Normale Superiore di Pisa and INFN Pisa, Italy

F. Benotto, N. Demaria, F. Dumitrache, R. Farano

INFN Torino, Italy

M.A. Borgia, R. Castello, M. Costa, E. Migliore, A. Romero

INFN and University of Torino, Italy

D. Abbaneo, M. Abbas,I. Ahmed, I. Akhtar, E. Albert, C. Bloch, H. Breuker, S. Butt,O. Buchmuller [j)], A. Cattai, C. Delaere[k)], M. Delattre,L. M. Edera, P. Engstrom, M. Eppard, M. Gateau, K. Gill, A.-S. Giolo-Nicollerat, R. Grabit, A. Honma, M. Huhtinen, K. Kloukinas, J. Kortesmaa, L. J. Kottelat, A. Kuronen, N. Leonardo, C. Ljuslin, M. Mannelli, L. Masetti, A. Marchioro, S. Mersi, S. Michal, L. Mirabito, J. Muffat-Joly, A. Onnela, C. Paillard, I. Pal, J. F. Pernot, P. Petagna, P. Petit, C. Piccut, M. Pioppi, H. Postema, R. Ranieri, D. Ricci, G. Rolandi, F. Ronga[l)], C. Sigaud, A. Syed, P. Siegrist, P. Tropea, J. Troska, A. Tsirou, M. Vander Donckt, F. Vasey

European Organization for Nuclear Research (CERN), Geneva, Switzerland

E. Alagoz, C. Amsler, V. Chiochia, C. Regenfus, P. Robmann, J. Rochet, T. Rommerskirchen, A. Schmidt, S. Steiner, L. Wilke

University of Zürich, Switzerland

I. Church, J. Cole[n)], J. Coughlan, A. Gay, S. Taghavi, I. Tomalin

STFC, Rutherford Appleton Laboratory, Chilton, Didcot, United Kingdom

R. Bainbridge, N. Cripps, J. Fulcher, G. Hall, M. Noy, M. Pesaresi, V. Radicci[n)], D. M. Raymond, P. Sharp[a)], M. Stoye, M. Wingham, O. Zorba

Imperial College, London, United Kingdom

I. Goitom, P. R. Hobson, I. Reid, L. Teodorescu

Brunel University, Uxbridge, United Kingdom

G. Hanson, G.-Y. Jeng, H. Liu, G. Pasztor[o)], A. Satpathy, R. Stringer

University of California, Riverside, California, USA

B. Mangano

University of California, San Diego, California, USA

K. Affolder, T. Affolder[p)], A. Allen, D. Barge, S. Burke, D. Callahan, C. Campagnari, A. Crook, M. D'Alfonso, J. Dietch, J. Garberson, D. Hale, H. Incandela, J. Incandela, S. Jaditz [q)], P. Kalavase, S. Kreyer, S. Kyre, J. Lamb, C. Mc Guinness[r)], C. Mills[s)], H. Nguyen, M. Nikolic[m)], S. Lowette, F. Rebassoo, J. Ribnik, J. Richman, N. Rubinstein, S. Sanhueza, Y. Shah, L. Simms[r)], D. Staszak[t)], J. Stoner, D. Stuart, S. Swain, J.-R. Vlimant, D. White

University of California, Santa Barbara, California, USA

K. A. Ulmer, S. R. Wagner

University of Colorado, Boulder, Colorado, USA

L. Bagby, P. C. Bhat, K. Burkett, S. Cihangir, O. Gutsche, H. Jensen, M. Johnson, N. Luzhetskiy, D. Mason, T. Miao, S. Moccia, C. Noeding, A. Ronzhin, E. Skup, W. J. Spalding, L. Spiegel, S. Tkaczyk, F. Yumiceva, A. Zatserklyaniy, E. Zerev

Fermi National Accelerator Laboratory (FNAL), Batavia, Illinois, USA

I. Anghel, V. E. Bazterra, C. E. Gerber, S. Khalatian, E. Shabalina

University of Illinois, Chicago, Illinois, USA

P. Baringer, A. Bean, J. Chen, C. Hinchey, C. Martin,T. Moulik, R. Robinson

University of Kansas, Lawrence, Kansas, USA

A. V. Gritsan, C. K. Lae, N. V. Tran

Johns Hopkins University, Baltimore, Maryland, USA

P. Everaerts, K. A. Hahn, P. Harris, S. Nahn, M. Rudolph, K. Sung

Massachusetts Institute of Technology, Cambridge, Massachusetts, USA

B. Betchart, R. Demina, Y. Gotra, S. Korjenevski, D. Miner, D. Orbaker

University of Rochester, New York, USA

L. Christofek, R. Hooper, G. Landsberg, D. Nguyen, M. Narain,T. Speer, K. V. Tsang

Brown University, Providence, Rhode Island, USA

---

[a] Also at CERN, European Organization for Nuclear Research, Geneva, Switzerland

[b] Now at University of Hamburg, Institute for Experimental Physics, Hamburg, Germany

[c] On leave from IFIN-HH, Bucharest, Romania

[d] Now at LLR-Ecole Polytechnique, France

[e] Now at Northeastern University, Boston, USA

[f] Now at IFIC, Centro mixto U. Valencia/CSIC, Valencia, Spain

[g] Now at Universiteit Antwerpen, Antwerpen, Belgium

[h] Now at ETH Zurich, Zurich, Switzerland

[i] Also Peking University, China

[j] Now at Imperial College, London, UK

[k] Now at Université catholique de Louvain, UCL, Louvain-la-Neuve, Belgium

[l] Now at Eidgenössische Technische Hochschule, Zürich, Switzerland

[m] Now at University of California, Davis, California, USA

[n] Now at Kansas University, USA

[o] Also at Research Institute for Particle and Nuclear Physics, Budapest, Hungary

[p] Now at University of Liverpool, UK

[q] Now at Massachusetts Institute of Technology, Cambridge, Massachusetts, USA

[r] Now at Stanford University, Stanford, California, USA

[s] Now at Harvard University, Cambridge, Massachusetts, USA

[t] Now at University of California, Los Angeles, California, USA

Abstract

The results of the CMS tracker alignment analysis are presented using the data from cosmic tracks, optical survey information, and the laser alignment system at the Tracker Integration Facility at CERN. During several months of operation in the spring and summer of 2007, about five million cosmic track events were collected with a partially active CMS Tracker. This allowed us to perform first alignment of the active silicon modules with the cosmic tracks using three different statistical approaches; validate the survey and laser alignment system performance; and test the stability of Tracker structures under various stresses and temperatures ranging from $+15^{\circ}$C to -15°C. Comparison with simulation shows that the achieved alignment precision in the barrel part of the tracker leads to residual distributions similar to those obtained with a random misalignment of 50 (80) μm in the outer (inner) part of the barrel.

Contents

1 Introduction

The all-silicon design of the CMS tracker poses new challenges in aligning a system with more than 15,000 independent modules. It is necessary to understand the alignment of the silicon modules to close to a few micron precision. Given the inaccessibility of the interaction region, the most accurate way to determine the silicon detector positions is to use the data generated by the silicon detectors themselves when they are traversed in-situ by charged particles. Additional information about the module positions is provided by the optical survey during construction and by the Laser Alignment System during the detector operation.

1.1 TIF Tracker and Goal of Alignment

A unique opportunity to gain experience in alignment of the CMS silicon strip tracker [1, 2] ahead of the installation at the underground cavern comes from tests performed at the Tracker Integration Facility (TIF). During several months of operation in the spring and summer of 2007, about five million cosmic track events were collected to tape. The tracker was operated with different coolant temperatures ranging from $+15°$C to $-15°$C. About 15% of the silicon strip tracker was powered and read-out simultaneously. An external trigger system was used to trigger on cosmic track events. The silicon pixel detector was only trial-inserted at TIF and was not involved in data taking.

In this note, we show alignment results primarily with the track-based approach, where three statistical algorithms have been employed showing consistent results. Assembly precision and structure stability with time are also studied. The experience gained in analysis of the TIF data will help evolving alignment strategies with tracks, give input into the stability of the detector components with temperature and assembly progress, and test the reliability of the optical survey information and the laser alignment system in anticipation of the first LHC beam collisions.

1.2 CMS Tracker Geometry

The CMS tracker is the largest silicon detector ever constructed. Even with about 15% of the silicon strip tracker activated during the TIF test, more than 2,000 individual modules were read out.

The strip detector of CMS is composed of four sub-detectors, as sketched in Fig. 1: the Tracker Inner and Outer Barrels (TIB and TOB), the Tracker Inner Disks (TID), and the Tracker Endcaps (TEC). They are all concentrically arranged around the nominal LHC beam axis that coincides with the z-axis. The right handed, orthogonal CMS coordinate system is completed by the x- and y-axes where the latter is pointing upwards. The polar and azimuthal angles ϕ and θ are measured from the positive x- and z-axis, respectively, whereas the radius r denotes the distance from the z-axis.

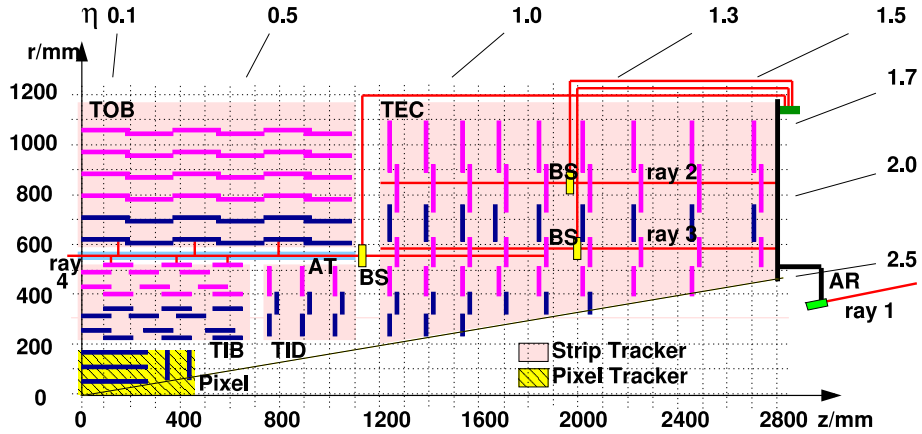

Figure 1: *A quarter of the CMS silicon tracker in an rz view. Single module positions are indicated as purple lines and dark blue lines indicate pairs of $r\phi$ and stereo modules. The path of the laser rays, the beam splitters (BS) and the alignment tubes (AT) of the Laser Alignment System are shown.*

The TIB and TOB are composed of four and six layers, respectively. Modules are arranged in linear structures parallel to the z-axis, which are named "strings" for TIB (each containing three modules) and "rods" for TOB (each containing six modules). The TID has six identical disk structures. The modules are arranged on both sides of ring-shaped concentric structures, numbering three per disk. Both TECs are built from nine disks, with eight

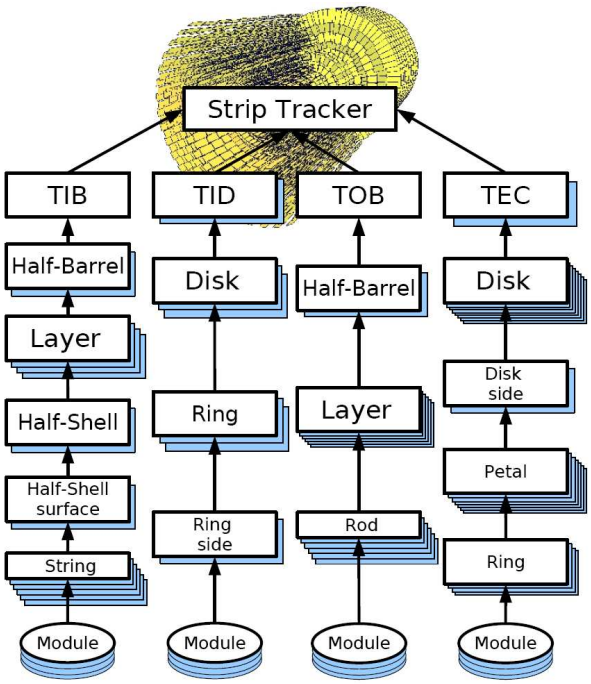

Figure 2: *Hierarchy of the CMS silicon strip detector structures.*

"front" and "back" "petals" alternatingly mounted on either side, with a petal being a wedge-shaped structure covering a narrow ϕ region and consisting of up to 28 modules, ordered in a ring structure as well. We outline the hierarchy of the Strip detector structures in Fig. 2.

Strips in the $r\phi$ modules have their direction parallel to the beam axis in the barrel and radially in the endcaps. There are also stereo modules in the first two layers or rings of all four sub-detectors (TIB, TOB, TID, TEC) and also in ring five of the TEC. The stereo modules are mounted back-to-back to the $r\phi$ modules with a stereo angle of 100 mrad and provide, when combining measurements with the $r\phi$ modules, a measurement of z in the barrel or r in the endcap. A pair of an $r\phi$ and a stereo module is also called a double-sided module. The strip pitch varies from 80 to 205 μm depending on the module, leading to single point resolutions of up to $23 - 53$ μm in the barrel [2].

2 Input to Alignment

In this section we discuss the input data for the alignment procedure of the CMS Tracker:

- charged particle tracks;
- optical survey prior to and during installation;
- laser alignment system measurements.

2.1 Data Samples, Tracking, and Event Selection

Track reconstruction and performance specific to the Tracker Integration Facility configuration are discussed in detail in Refs. [3, 4].

Three different trigger configurations were used in TIF data-taking, called A, B and C and shown in Fig. 3. About 15% of the detector modules, all located at $z > 0$, were powered and read-out. This includes 444 modules in TIB (16%), 720 modules in TOB (14%), 204 modules in TID (25%), and 800 modules in TEC (13%). Lead plates were included above the lower trigger scintillators, which enforced a minimum energy of the cosmic rays of 200 MeV to be triggered.

The data were collected in trigger configuration A at room temperature ($+15$°C), both before and after insertion of the TEC at $z < 0$. All other configurations (B and C) had all strip detector components integrated. In addition to

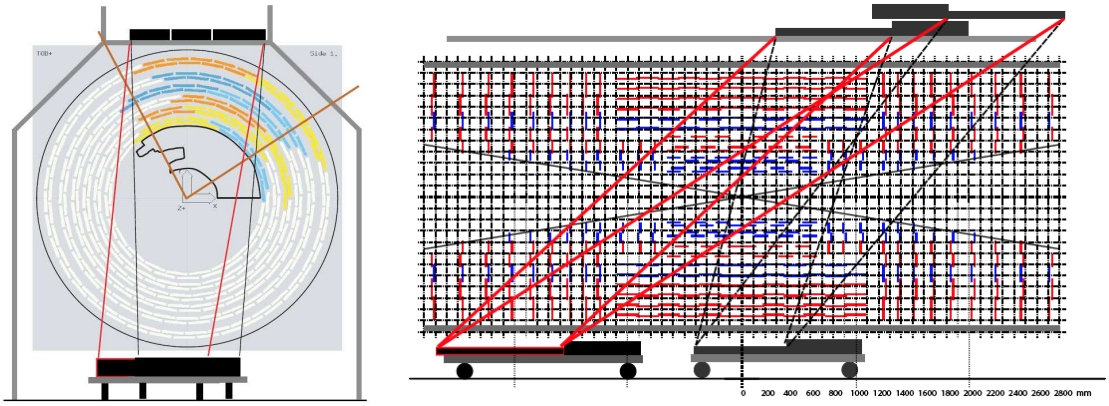

Figure 3: *Layout of the CMS Strip Tracker and of the trigger scintillators at TIF. The acceptance region is indicated by the straight lines connecting the active areas of the scintillators. Configuration A corresponds approximately to the acceptance region defined by the forward (right) bottom scintillator; configuration B corresponds to the left bottom scintillator; and configuration C combines both of the above.*

Label	Trigger Position	Temperature	N_{trig}	
A_1	A	15°C	665 409	before TEC- insertion
A_2	A	15°C	189 925	after TEC- insertion
B	B	15°C	177 768	
C_{15}	C	15°C	129 378	
C_{10}	C	10°C	534 759	
C_0	C	-1°C	886 801	
C_{-10}	C	-10°C	902 881	
C_{-15}	C	-15°C	655 301	less modules read out
C_{14}	C	14°C	112 134	
MC	C	–	3 091 306	simulation

Table 1: *Overview of different data sets, ordered in time, and their number of triggered events N_{trig} taking into account only good running conditions.*

room temperature, configuration C was operated at +10 °C, -1 °C, -10 °C, and -15 °C. Due to cooling limitations, a large number of modules had to be turned off at -15 °C. The variety of different configurations allows us to study alignment stability with different stress and temperature conditions. Table 1 gives an overview of the different data sets.

We also validate tracking and alignment algorithm performances with simulation. A sample of approximately three million cosmic track events was simulated using the CMSCGEN simulator [5]. Only cosmic muon tracks within specific geometrical ranges were selected to simulate the scintillator trigger configuration C. To extend CMSCGEN's energy range, events at low muon energy have been re-weighted to adjust the energy spectrum to the CAPRICE data [6].

Charged track reconstruction includes three essential steps: seed finding, pattern recognition, and track fitting. Several pattern recognition algorithms are employed on CMS, such as "Combinatorial Track Finder" (CTF), "Road Search", and "Cosmic Track Finder", the latter being specific to the cosmic track reconstruction. All three algorithms use the Kalman filter algorithm for final track fitting, but the first two steps are different. The track model used is a straight line parametrised by four parameters where the Kalman filter track fit includes multiple scattering effects in each crossed layer. We employ the CTF algorithm for alignment studies in this note.

In order to recover tracking efficiency which is otherwise lost in the pattern recognition phase because hits are moved outside the standard search window defined by the detector resolution, an "alignment position error" (APE) is introduced. This APE is added quadratically to the hit resolution, and the combined value is subsequently used as a search window in the pattern recognition step. The APE settings used for the TIF data are modelling the assembly tolerances [2].

There are several important aspects of the TIF configuration which require special handling with respect to normal data-taking. First of all, no magnetic field is present. Therefore, the momentum of the tracks cannot be measured and estimates of the energy loss and multiple scattering can be done only approximately. A track momentum of 1 GeV/c is assumed in the estimates, which is close to the average cosmic track momentum observed in simulated spectra. Other TIF-specific features are due to the fact that the cosmic muons do not originate from the interaction region. Therefore the standard seeding mechanism is extended to use also hits in the TOB and TEC, and no beam spot constraint is applied. For more details see Ref. [3].

Reconstruction of exactly one cosmic muon track in the event is required. A number of selection criteria is applied on the hits, tracks, and detector components subject to alignment, to ensure good quality data. This is done based on trajectory estimates and the fiducial tracking geometry. In addition, hits from noisy clusters or from combinatorial background tracks are suppressed by quality cuts on the clusters. The detailed track selection is as follows:

- The direction of the track trajectory satisfies the requirements: $-1.5 < \eta_{track} < 0.6$ and $-1.8 < \phi_{track} < -1.2$ rad, according to the fiducial scintillator positions.
- The χ^2 value of the track fit, normalised to the number of degrees of freedom, fulfils $\chi^2_{track}/\text{ndof} < 4$.
- The track has at least 5 hits associated and among those at least 2 matched hits in double-sided modules.

A hit is kept for the track fit:

- If it is associated to a cluster with a total charge of at least 50 ADC counts. If the hit is matched, both components must satisfy this requirement.
- If it is isolated, i.e. if any other reconstructed hit is found on the same module within 8.0 mm, the whole track is rejected. This cut helps in rejecting fake clusters generated by noisy strips and modules.
- If it is not discarded by the outlier rejection step during the refit (see below).

The remaining tracks and their associated hits are refit in every iteration of the alignment algorithms. An outlier rejection technique is applied during the refit. Its principle is to iterate the final track fit until no outliers are found. An outlier is defined as a hit whose trajectory estimate is larger than a given cut value ($e_{cut} = 5$). The trajectory estimate of a hit is the quantity: $e = \mathbf{r}^T \cdot \mathbf{V}^{-1} \cdot \mathbf{r}$, where $\mathbf{r}$ is the 1- or 2-dimensional local residual vector and $\mathbf{V}$ is the associated covariance matrix. If one or more outliers are found in the first track fit, they are removed from the hit collection and the fit is repeated. This procedure is iterated until there are no more outliers or the number of surviving hits is less than 4.

Unless otherwise specified, these cuts are common to all alignment algorithms used. The combined efficiency for all the cuts above is estimated to be 8.3% on TIF data (the C_{-10} sample is used in this estimate) and 20.5% in the TIF simulation sample.

2.2 Survey of the CMS Tracker

Information about the relative position of modules within detector components and of the larger-level structures within the tracker is available from the optical survey analysis prior to or during the tracker integration. This includes Coordinate Measuring Machine (CMM) data and photogrammetry, the former usually used for the active element measurements and the latter for the larger object alignment. For the inner strip detectors (TIB and TID), survey data at all levels was used in analysis. For the outer strip detectors (TOB and TEC), module-level survey was used only for mounting precision monitoring, while survey of high-level structures was used in analysis.

For TIB, survey measurements are available for the module positions with respect to shells, and of cylinders with respect to the tracker support tube. Similarly, for TID, survey measurements were done for modules with respect to the rings, rings with respect to the disks and disks with respect to the tracker support tube. For TOB, the wheel was measured with respect to the tracker support tube. For TEC, measurements are stored at the level of disks with respect to the endcaps and endcaps with respect to the tracker support tube.

Figure 4 illustrates the relative positions of the CMS tracker modules with respect to design geometry as measured in optical survey: as can be seen, differences from design geometry as large as several millimetres are expected. Since hierarchical survey measurements were performed and TOB and TEC have only large-structure information, the corresponding modules appear to be coherently displaced in the plot.

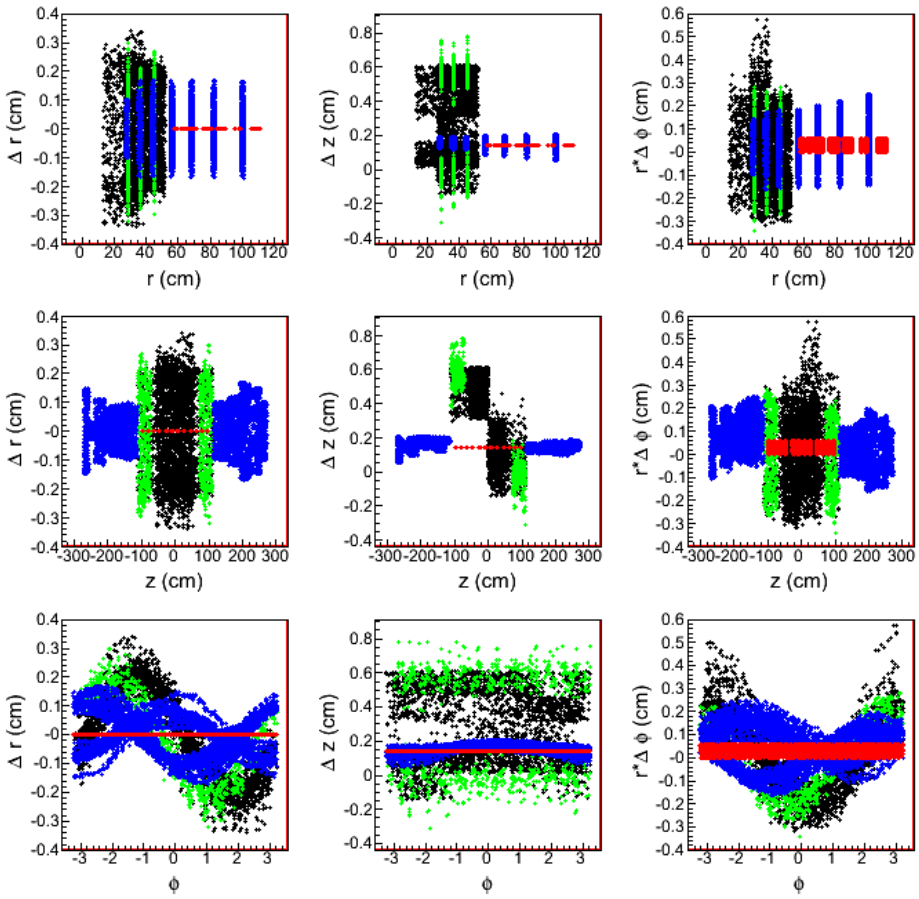

Figure 4: *Displacement of modules in global cylindrical coordinates as measured in survey with respect to design geometry. A colour coding is used: black for TIB, green for TID, red for TOB, and blue for TEC.*

2.3 Laser Alignment System of the CMS Tracker

The Laser Alignment System (LAS) uses infrared laser beams with a wavelength of $\lambda = 1075\,\text{nm}$ to monitor the position of selected tracker modules. It operates globally on tracker substructures (TIB, TOB and TEC disks) and cannot determine the position of individual modules. The goal of the system, already sketched in Fig. 1, is to generate alignment information on a continuous basis, providing geometry reconstruction of the tracker substructures at the level of $100\,\mu\text{m}$. In addition, possible tracker structure movements can be monitored at the level of $10\,\mu\text{m}$, providing additional input for the track based alignment.

In each TEC, laser beams cross all nine TEC disks in ring 6 and ring 4 on the back petals, equally distributed in ϕ. Here, special silicon sensors with a $10\,\text{mm}$ hole in the backside metallisation and an anti-reflective coating are mounted. The beams are used for the internal alignment of the TEC disks. The other eight beams, distributed in ϕ, are foreseen to align TIB, TOB, and both TECs with respect to each other. Finally, there is a link to the muon system, which is established by 12 laser beams (six on each side) with precise position and orientation in the tracker coordinate system.

The signal induced by the laser beams on the silicon sensors decreases in height as the beams penetrate through subsequent silicon layers in the TECs and through beam splitters in the alignment tubes that partly deflect the beams onto TIB and TOB sensors. To obtain optimal signals on all sensors, a sequence of laser pulses with increasing intensities, optimised for each position, is generated. Several triggers per intensity are taken and the signals are averaged. In total, a few hundred triggers are needed to get a full picture of the alignment of the tracker structure. Since the trigger rate for the alignment system is around $100\,\text{Hz}$, this takes only a few seconds.

3 Statistical Methods and Approaches

All the methods use a common definition of module coordinates for alignment. A module is assumed to be a rigid body, so three absolute positions and three rotations are sufficient to express its degrees of freedom, illustrated in Fig. 5. Thus, the final goal of the alignment procedure is to obtain six parameters for each independent module, these being the three spatial and three rotational parameters.

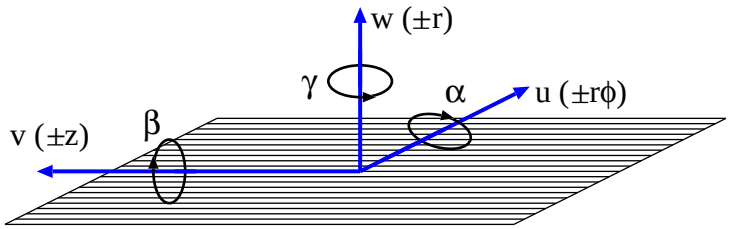

Figure 5: Schematic illustration of the local coordinates of a module as used for alignment. Global parameters (in parentheses) are shown for modules in the barrel detectors (TIB and TOB).

The local positions are called u, v and w, where u is along the sensitive coordinate (i.e. across the strips), v is perpendicular to u in the sensor plane and w is perpendicular to the uv-plane, completing the right-handed coordinate system. The rotations around the u, v and w axes are called α, β and γ, respectively. In the case of alignment of intermediate structures like rods, strings or petals, we follow the convention that u and v are parallel and perpendicular to the precisely measured coordinate, while for the large structures like layers and disks, the local coordinates coincide with the global ones.

3.1 Alignment Concepts

Alignment analysis with tracks uses the fact that the hit positions and the measured trajectory impact points of a track are systematically displaced if the module position is not known correctly. The difference in local module coordinates between these two quantities are the *track-hit residuals* $\mathbf{r}_i$, which are 1- (2-dimensional) vectors in the case of a single (double) sided module and which one would like to minimise. More precisely, one can minimise the χ^2 function which includes a covariance matrix $\mathbf{V}$ of the measurement uncertainties:

$$\chi^2 = \sum_{i}^{\text{hits}} \mathbf{r}_i^T(\mathbf{p},\mathbf{q})\mathbf{V}_i^{-1}\mathbf{r}_i(\mathbf{p},\mathbf{q}) \tag{1}$$

where $\mathbf{p}$ represents the position and orientation of the modules and $\mathbf{q}$ represents the track parameters.

There are different alignment methods used to minimise Eq. (1). It can be solved either directly or by minimising subsets of the parameters (a local method, e.g. per module) over iterations. In this section, we discuss the three statistical methods used for track-based alignment in this analysis.

- Hits and Impact Points (HIP) local iterative method;
- Kalman filter fit method;
- Millepede global minimisation method.

3.1.1 HIP algorithm

The HIP (Hits and Impact Points) algorithm is described in detail in Ref. [7], where its application to the pixel detectors with simulated collision data is studied. The solution of the χ^2 minimisation in Eq. (1) can be found in the general formalism with the linear approximation for the alignment parameters $\mathbf{p}_m$ of each module independently:

$$\mathbf{p}_m = \left[\sum_{i}^{\text{hits}} \mathbf{J}_i^T\mathbf{V}_i^{-1}\mathbf{J}_i\right]^{-1}\left[\sum_{i}^{\text{hits}} \mathbf{J}_i^T\mathbf{V}_i^{-1}\mathbf{r}_i\right] \tag{2}$$

where the Jacobian $\mathbf{J}_i$ is defined as the derivative of the residual with respect to the sensor position parameters and can be found analytically. The Jacobian is a matrix $N \times 6$, where N is the residual dimension. In the case of 1D or 2D track-hit residuals $\mathbf{r}_i$, the Jacobian $\mathbf{J}_i$ can be computed with the small angle approximation. Correlations between different modules and effects on the track parameters are neglected in Eq. (2). They are accounted for by iterating the minimisation process and by refitting the tracks with new alignment constants after each iteration.

3.1.2 Kalman filter algorithm

The Kalman alignment algorithm [8] is a sequential method, derived using the Kalman filter formalism. It is sequential in the sense that the alignment parameters are updated after each processed track. This allows it to use the current estimates directly for tracking. Furthermore, by processing more and more tracks traversing different sets of alignable objects, statistical correlations between the alignable objects evolve with each update. Due to these correlations, the updates are not restricted to the alignable objects that were crossed by the current track, but include also all other alignable objects.

The Kalman alignment algorithm is based on the track model $\boldsymbol{m} = \boldsymbol{f}(\boldsymbol{q}_t, \boldsymbol{p}_t) + \boldsymbol{\varepsilon}$. This model relates the observations $\boldsymbol{m}$ to the true track parameters $\boldsymbol{q}_t$ and the true alignment constants $\boldsymbol{p}_t$ via the deterministic function $\boldsymbol{f}$. Energy loss is considered to be deterministic and is dealt with in the track model. The stochastic vector $\boldsymbol{\varepsilon}$ as well as its variance-covariance matrix $\boldsymbol{V}$ contain the effects of the observation error and of multiple scattering. Therefore the matrix $\boldsymbol{V}$ contains correlations between hits such that equation (1) is a sum over tracks, with residuals being of higher dimension according to the number of hits along the track trajectory. Linearised around an expansion point $(\boldsymbol{q}_0, \boldsymbol{p}_0)$, i.e. track parameters from a preliminary track fit and an initial guess for the alignment constants, the track model reads:

$$\boldsymbol{m} = \boldsymbol{c} + \boldsymbol{D}_q \boldsymbol{q}_t + \boldsymbol{D}_p \boldsymbol{p}_t + \boldsymbol{\varepsilon}, \tag{3}$$

with

$$\boldsymbol{D}_q = \partial \boldsymbol{f} / \partial \boldsymbol{q}_t \big|_{\boldsymbol{q}_0}, \quad \boldsymbol{D}_p = \partial \boldsymbol{f} / \partial \boldsymbol{p}_t \big|_{\boldsymbol{p}_0}, \quad \boldsymbol{c} = \boldsymbol{f}(\boldsymbol{q}_0, \boldsymbol{p}_0) - \boldsymbol{D}_q \boldsymbol{q}_0 - \boldsymbol{D}_p \boldsymbol{p}_0 \tag{4}$$

By applying the Kalman filter formalism to this relation, updated equations for the alignment parameters $\boldsymbol{p}$ and their variance-covariance matrix $\boldsymbol{C}_p$ can be extracted. At step k, these equations read:

$$\boldsymbol{p}_{k+1} = \boldsymbol{p}_k + \boldsymbol{C}_{p,k} \boldsymbol{D}_p^{\mathrm{T}} \boldsymbol{G}_k \left(\boldsymbol{m} - \boldsymbol{c} - \boldsymbol{D}_p \, \boldsymbol{p}_k \right), \tag{5}$$

$$\begin{aligned} \boldsymbol{C}_{p,k+1} = & \left(\boldsymbol{I} - \boldsymbol{C}_{p,k} \boldsymbol{D}_p^{\mathrm{T}} \boldsymbol{G}_k \, \boldsymbol{D}_p \right) \boldsymbol{C}_{p,k} \left(\boldsymbol{I} - \boldsymbol{D}_p^{\mathrm{T}} \boldsymbol{G}_k \, \boldsymbol{D}_p \, \boldsymbol{C}_{p,k} \right) \\ & + \boldsymbol{C}_{p,k} \boldsymbol{D}_p^{\mathrm{T}} \boldsymbol{G}_k \, \boldsymbol{V} \boldsymbol{G}_k \, \boldsymbol{D}_p \, \boldsymbol{C}_{p,k} \end{aligned} \tag{6}$$

with

$$\boldsymbol{G}_k^{-1} = \boldsymbol{V}_k^{-1} - \boldsymbol{V}_k^{-1} \boldsymbol{D}_q \left(\boldsymbol{D}_q^{\mathrm{T}} \boldsymbol{V}_k^{-1} \boldsymbol{D}_q \right)^{-1} \boldsymbol{D}_q^{\mathrm{T}} \boldsymbol{V}_k^{-1} \quad \text{and} \quad \boldsymbol{V}_k = \boldsymbol{V} + \boldsymbol{D}_p \, \boldsymbol{C}_{p,k} \boldsymbol{D}_p^{\mathrm{T}}.$$

3.1.3 Millepede algorithm

Millepede II is an upgraded version of the Millepede program [9]. Its principle is the χ^2 function minimisation, simultaneously taking into account track and alignment parameters. Since angular corrections are small, the linearised problem is a good approximation for alignment. Being interested only in the n alignment parameters, the problem is reduced to the solution of a matrix equation of size n.

Depending on the size and the sparseness of the matrix, there are several methods implemented in Millepede II [10] to solve the equation for up to $n = 100\,000$. Hit outlier rejection and down-weighting as well as constraints to fix e.g. the global degrees of freedom turn out to be important. Millepede II has been used successfully in the first full CMS tracker alignment study on simulated data [11].

The χ^2 function, Eq. (1), depends on track (local) and alignment (global) parameters. Denoting global parameters by the vector $\mathbf{p}$ and local parameters of track j by the vector $\mathbf{q}_j$, the global χ^2 function can be expressed as the sum of local χ^2 contributions,

$$\chi^2(\mathbf{p}, \mathbf{q}) = \sum_{j}^{\text{tracks}} \chi^2_j(\mathbf{p}, \mathbf{q}_j). \tag{7}$$

The local $\chi^2_j(\mathbf{p}, \mathbf{q}_j)$ can be written in terms of residuals between the uncorrelated measured hit positions y_i and their corresponding prediction $f_i(\mathbf{p}, \mathbf{q_j})$ of the track model, weighted by the inverse of the standard deviation σ_i of the hit measurement,

$$\chi^2_j(\mathbf{p}, \mathbf{q}_j) = \sum_{i}^{\text{hits}} \frac{\left(y_i - f_i(\mathbf{p}, \mathbf{q}_j) \right)^2}{\sigma_i^2}. \tag{8}$$

Given reasonable start values $\mathbf{p}_0$ and $\mathbf{q}_{j0}$ as expected in alignment, the track model prediction $f_i(\mathbf{p}, \mathbf{q}_j)$ can be linearised. Equation 8 becomes

$$\chi^2_j(\mathbf{p}, \mathbf{q}_j) \approx \sum_i^{\text{hits}} \frac{\left(y_i - f_i(\mathbf{p}_0, \mathbf{q}_{j0}) + \frac{\partial f_i}{\partial \mathbf{p}}\mathbf{a} + \frac{\partial f_i}{\partial \mathbf{q}_j}\Delta\mathbf{q}_j\right)^2}{\sigma_i^2}, \tag{9}$$

where the alignment parameters $\mathbf{a} = \Delta\mathbf{p}$ denote the small correction to the global parameters and $\Delta\mathbf{q}_j$ the correction to the local parameters.

Using this linearision, $\sum_j \chi^2_j$ can be minimised using the least squares method. This results in a large linear system with one equation for each alignment parameter and all the track parameters of each track. But since the parameterisation of a track k is independent of the parameters of track j ($\partial f_i^k / \partial \mathbf{q}_j = 0$, $k \neq j$), the particular structure of the system of equations allows a reduction of its size, leading to a matrix equation

$$\mathbf{C}\,\mathbf{a} = \mathbf{b}, \tag{10}$$

where the matrix C is built from the derivatives $\partial f_i / \partial \mathbf{q}_j$ and $\partial f_i / \partial \mathbf{p}$ and the vector $\mathbf{b}$ from the derivatives and the residuals $(y_i - f_i(\mathbf{p}_0, \mathbf{q}_{j0}))$, all normalised to the uncertainties σ_i.

3.1.4 Limitations of alignment algorithms

We should note that Eq. (1) may be invariant under certain coherent transformations of assumed module positions, the so-called "weak" modes. The trivial transformation which is χ^2-invariant is a global translation and rotation of the whole tracker. This transformation has no effect in internal alignment, and is easily resolved by a suitable convention for defining the global reference frame. Different algorithms employ different approaches and conventions here, so we will discuss this in more detail as it applies to each algorithm.

The non-trivial χ^2-invariant transformations which preserve Eq. (1) are of larger concern. For the full CMS tracker with cylindrical symmetry one could define certain "weak" modes, such as elliptical distortion, twist, etc., depending on the track sample used. However, since we use only a partial CMS tracker without the full azimuthal coverage, different "weak" modes may show up. For example, since we have predominantly vertical cosmic tracks (along the global y axis), a simple shift of all modules in the y direction approximately constitutes a "weak" mode, this transformation preserving the size of the track residuals for a vertical track. However, since we still have tracks with some angle to vertical axis, some sensitivity to the y coordinate remains.

In general, any particular track sample would have its own "weak" modes and the goal of an unbiased alignment procedure is to remove all χ^2-invariant transformations with a balanced input of different kinds of tracks. In this study we are limited to only predominantly vertical single cosmic tracks and this limits our ability to constrain χ^2-invariant transformations, or the "weak" modes. This is discussed more in the validation section.

3.2 Application of Alignment Algorithms to the TIF Analysis

Accurate studies have been performed with all algorithms in order to determine the maximal set of detectors that can be aligned and the aligned coordinates that are sensitive to the peculiar track pattern and limited statistics of TIF cosmic track events.

For the tracker barrels (TIB and TOB), the collected statistics is sufficient to align at the level of single modules if restricting to a geometrical subset corresponding to the positions of the scintillators used for triggering. The detectors aligned are those whose centres lie inside the geometrical ranges,

- $z > 0$,
- $x < 75$ cm and
- $0.5 < \phi < 1.7$ rad

where all the coordinates are in the global CMS frame.

The local coordinates aligned for each module are

- u, v, γ for TOB double-sided modules,

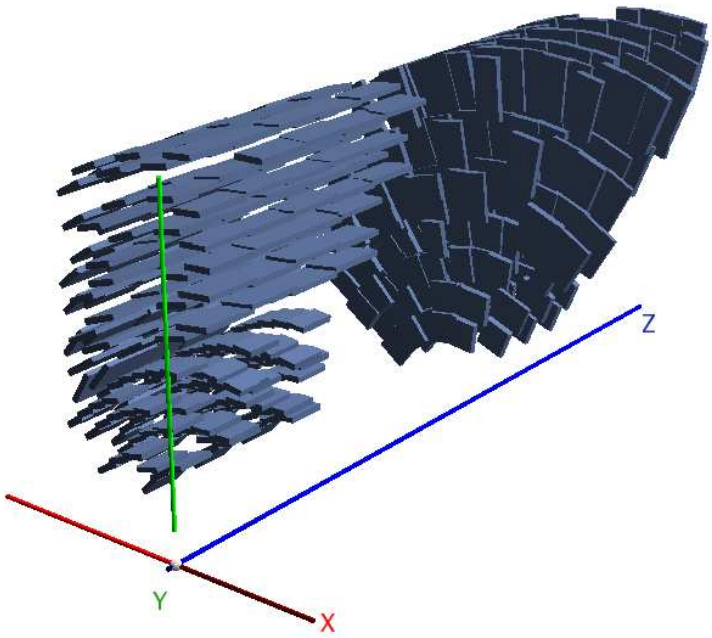

Figure 6: *Visualisation of the modules used in the track-based alignment procedure. Selected modules based on the common geometrical and track-based selection for the algorithms.*

- u, γ for TOB single-sided modules,
- u, v, w, γ for TIB double-sided modules and
- u, w, γ for TIB single-sided modules.

Due to the rapidly decreasing cosmic track rate $\sim \cos^2 \psi$ (with ψ measured from zenith) only a small fraction of tracks cross the endcap detector modules at an angle suitable for alignment. Therefore, the z^+-side Tracker endcap (TEC) could only be aligned at the level of disks. All nine disks are considered in TEC alignment, and the only aligned coordinate is the angle $\Delta\phi$ around the CMS z-axis. Because there are only data in two sectors of the TEC, the track-based alignment is not sensitive to the x and y coordinates of the disks.

The Tracker Inner Disks (TID) are not aligned due to lack of statistics. Figure 6 visualises the modules selected for the track-based alignment procedure.

3.2.1 HIP algorithm

Preliminary residual studies show that, in real data, the misalignment of the TIB is larger than in TOB, and TEC alignment is quite independent from that of other structures. For this reason, the overall alignment result is obtained in three steps:

1. In the first step, the TIB is excluded from the analysis and the tracks are refit using only reconstructed hits in the TOB. Alignment parameters are obtained for this subdetector only. No constraints are applied on the global coordinates of the TOB as a whole.
2. In the second step, the tracks are refit using all their hits; the TOB is fixed to the positions found after step 1 providing the global reference frame; and alignment parameters are obtained for TIB only.
3. The alignment of the TEC is then performed as a final step starting from the aligned barrel geometry found after steps 1 and 2.

Selection of aligned objects and coordinates is done according to the common criteria described in Secs. 2.1 and 3.2.

The Alignment Position Error (APE) for the aligned detectors is set at the first iteration to a value compatible with the expected positioning uncertainties after assembly, then decreased linearly with the iteration number, reaching zero at iteration n (n varies for different alignment steps). Further iterations are then run using zero APE.

In order to avoid a bias in track refitting from parts of the TIF tracker that are not aligned in this procedure (e.g. low-ϕ barrel detectors), an arbitrarily large APE is assigned for all iterations to trajectory measurements whose corresponding hits lie in these detectors, de-weighting them in the χ^2 calculation.

For illustrative purposes, we show here the results of HIP alignment on the C_{-10} TIF data sample after event selection. Figures 7 to 9 show the evolution of the aligned positions and the alignment parameters calculated by the HIP algorithm after every iteration for the three alignment steps described above. We observe reasonable convergence for the coordinates that are expected to be most precisely determined (see Sec. 4.3) and a stable result in subsequent iterations using zero APE.

3.2.2 Kalman filter algorithm

In the barrel, the alignment is carried out starting from the module survey geometry. The alignment parameters are calculated for all modules in the TIB and the TOB at once, using the common alignable selection described in Sec. 3.2. No additional alignable selection criteria, for instance a minimum number of hits per module, is used. Due to the lack of any external aligned reference system, some global distortions in the final alignment can show up, e.g. shearing or rotation with respect to the true geometry.

The tracking is adapted to the needs of the algorithm, especially to include the current estimate of the alignment parameters. Since for every module the position error can be calculated from the up-to-date parameter errors, no additional fixed Alignment Position Error (APE) is used. The material effects are crudely taken into account by assuming a momentum of 1.5 GeV/c, which is larger than the one used in standard track reconstruction.

For TEC alignment a slightly modified Kalman filter algorithm is used. The procedure is split in two parts: The first part, using the CMS software, is in charge of the track reconstruction and the calculation of track and alignment derivatives, residuals and covariance matrices which subsequently are stored in ROOT files. This step can easily be parallelised. The second part includes the Kalman filter alignment algorithm and calculates the alignment parameters from the previously stored ROOT files. Outlying tracks, which would cause unreasonably large changes of the alignment parameters if used by the algorithm, are discarded.

Using this algorithm, an alignment on disk level is determined. Due to the experimental setup, the total number of hits per disk decreases such that the error on the calculated parameter increases from disk one to disk nine.

During the alignment process, disk 1 is used as reference. After that, the alignment parameters are transformed into the coordinate system defined by fixing the mean and slope of $\phi(z)$ to zero. This is done because there is no sensitivity to a linear torsion, which, in a linear approximation corresponds to a slope in $\phi(z)$, expected for the TEC. Due to differences in the second order approximation between a track inclination and a torsion of the TEC, the algorithm basically has a small sensitivity to a torsion of the endcap. Here, the linear component is expected to be superimposed into movements of the disks in x and y, which are converted by the algorithm into rotations because these are the only free parameters.

The alignment parameters do not seem to depend strongly on the temperature (see section 5.2), so all data except for the runs at -15 °C were merged to increase the statistics. The evolution of $\Delta\phi$ for these data is displayed in Fig. 10.

3.2.3 Millepede algorithm

Millepede alignment is performed at module level in both TIB and TOB, and at disk level in the TEC, in one step only. To fix the six degrees of freedom from global translation and rotation, equality constraints are used on the parameters in the TOB: These inhibit overall shifts and rotations of the TOB, while the TIB parameters are free to adjust to the fixed TOB position. In addition, TEC disk one is kept as fixed.

The requirements to select a track useful for alignment are described in Sec. 2.1. All these criteria are applied, except for the hit outlier rejection since outlier down-weighting is applied within the minimisation process. Since Millepede internally refits the tracks, it is additionally required that a track hits at least five of those modules which are subject to the alignment procedure. Multiple scattering and energy loss effects are treated, as in the Kalman filter alignment algorithm, by increasing and correlating the hit uncertainties, assuming a track momentum of 1.5 GeV/c. This limits the accuracy of the assumption of uncorrelated measured hit positions in Eq. (8).

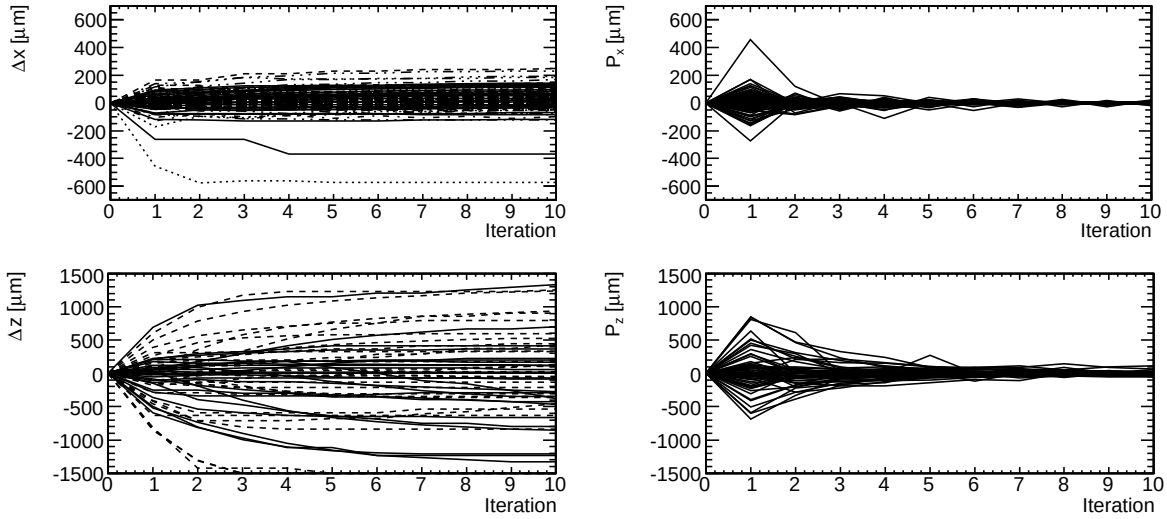

Figure 7: *Results of the first HIP alignment step (TOB modules only) on the C_{-10} TIF data sample. From top to bottom the plots show respectively the quantities Δx for all modules and Δz for double-sided modules (which are the two coordinates most precisely determined, see Sec. 4.3) where Δ stands for the difference between the aligned local position of a module at a given iteration of the algorithm and the nominal position of the same module. On the left column the evolution of the object position is plotted vs. the iteration number (different line styles correspond to the 6 TOB layers), while on the right the parameter increment for each iteration of the corresponding alignment parameters is shown.*

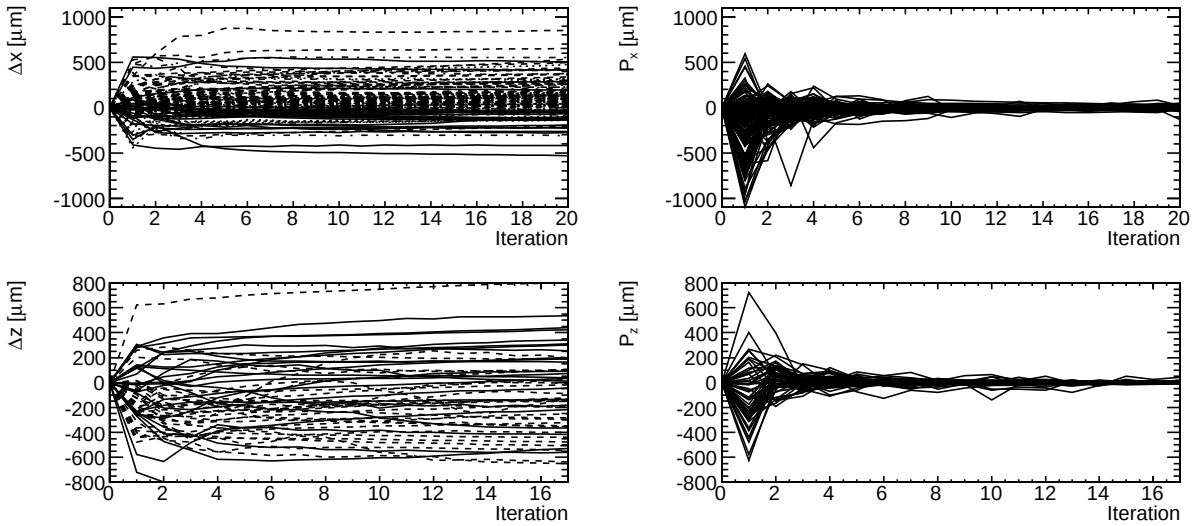

Figure 8: *Results of the second HIP alignment step (TIB modules after TOB alignment) on the C_{-10} TIF data sample. From top to bottom the plots show respectively the quantities Δx for all modules and Δz for double-sided modules (see caption of Fig. 7) On the left column the evolution of the object position is plotted vs. the iteration number (different line styles correspond to the 4 TIB layers), while on the right the parameter increment for each iteration of the corresponding alignment parameters is shown.*

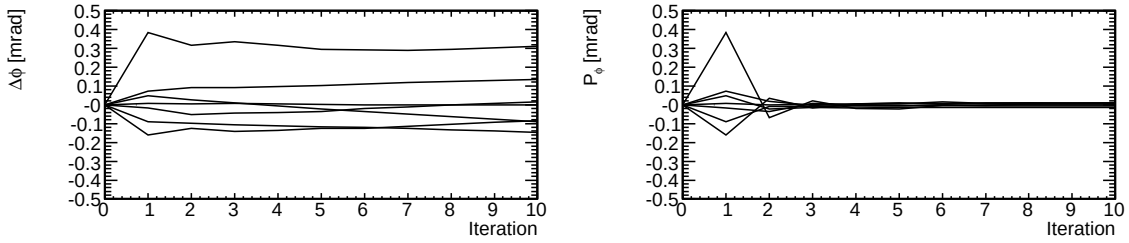

Figure 9: *Results of the third HIP alignment step (TEC discs after barrel alignment) on the C_{-10} TIF data sample. The plots show the quantity $\Delta\phi$. On the left column the evolution of the object position is plotted vs. the iteration number, while on the right the parameter increment for each iteration of the corresponding alignment parameters is shown, to estimate convergence quality.*

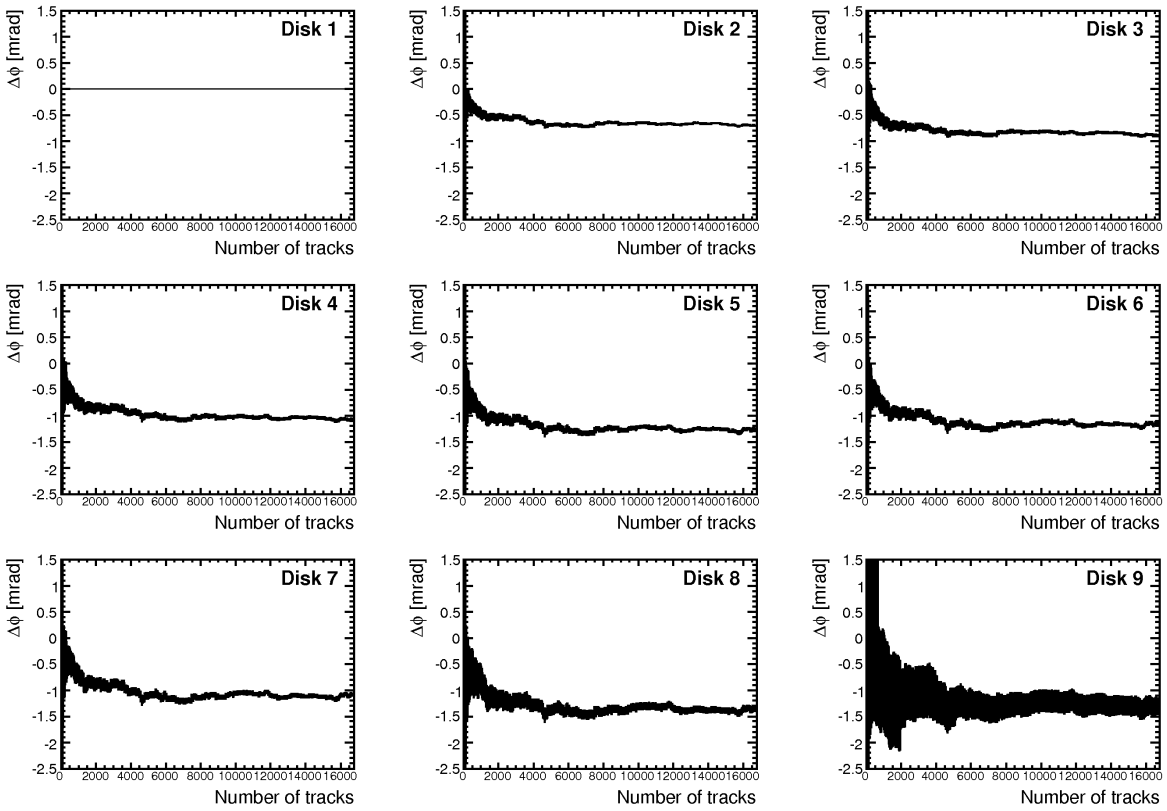

Figure 10: *Evolution of $\Delta\phi$ for the nine TEC disks. Disk 1 is fixed during the alignment process to define the coordinate system and hence remains at zero.*

The alignment parameters are calculated for all modules using the common alignable selection described in Sec. 3.2. Due to the fact that barrel and endcap are aligned together in one step, no request on the minimum number of hits in the subdetector for a selected track is done.

The required minimum number of hits for a module to be aligned is set to 50. Due to the modest number of parameters, the matrix equation (10) is solved by inversion, with five Millepede global iterations for the solution of Eq. (10), updating its right hand side with previously achieved alignment parameters. In each global iteration, the track fits are repeated four times. Except for the first iteration, Eq. (9) is modified assigning down-weighting factors for each hit depending on its normalised residuum of the previous fit (details see [10]). About 0.5% of the tracks with an average hit weight below 0.8 are rejected completely.

Fig. 11 shows, on the left, the number of hits per alignment parameter used for the global minimisation; 58 modules

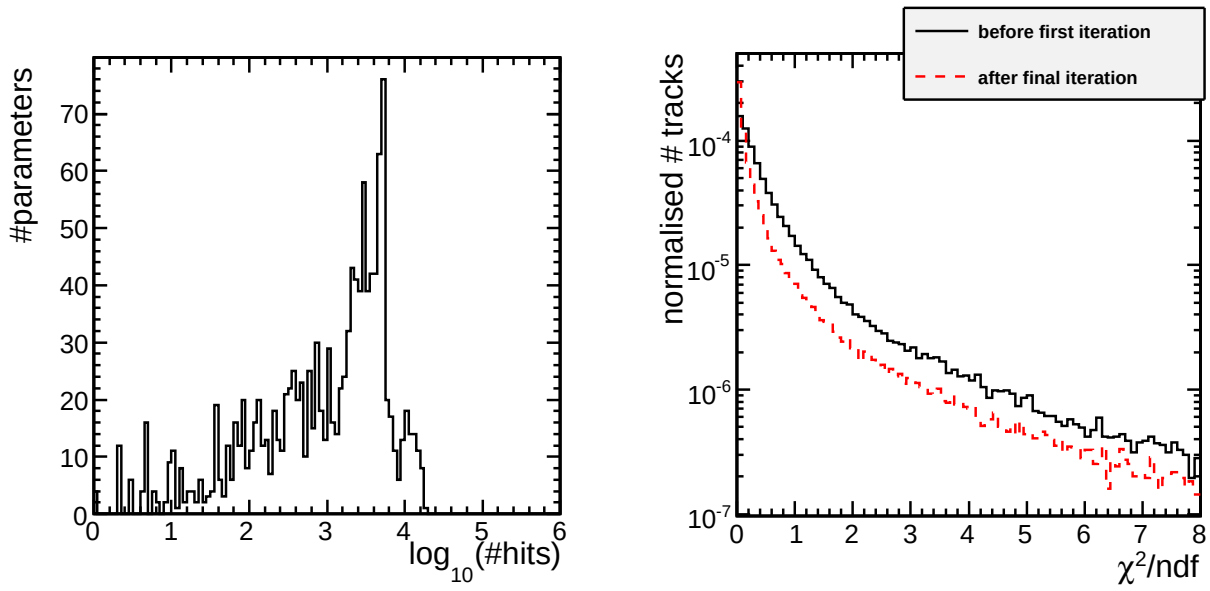

Figure 11: *Number of hits for the parameters aligned with Millepede (left) and improvement of the normalised χ^2 distribution as seen by Millepede (right).*

fail the cut of 50 hits. On the right, the normalised χ^2 distributions of the Millepede internal track fits before and after minimisation are shown. The distributions do not have a peak close to one, indicating that the hit uncertainties are overestimated. Nevertheless, the effect of minimisation can clearly be seen.

4 Validation of Alignment of the CMS Tracker at TIF

In this section we present validation of the alignment results. Despite the limited precision of alignment that prevents detailed systematic distortion studies, the available results from TIF provide important validation of tracker alignment for the set of modules used in this study.

The evolution of the module positions is shown starting from the design geometry, moving to survey measurements, and finally comparing to the results from the track-based algorithms. Both the overall track quality and individual hit residuals improve between the three steps. All three track-based algorithms produce similar results when the same input and similar approaches are taken. We show that the residual misalignments are consistent with statistical uncertainties in the procedure. Therefore, we pick just one alignment geometry from the track-based algorithms for illustration of results when comparison between different algorithms is not relevant.

4.1 Validation Methods

We use two methods in validation and illustration of the alignment results. One approach is track-based and the other approach directly compares geometries resulting from different sets of alignment constants.

In the track-based approach, we refit the tracks with all Alignment Position Errors (APE) set to zero. A loose track selection is applied, requiring at least six hits where more than one of them must be two-dimensional. Hit residuals will be shown as the difference between the measured hit position and the track position on the module plane. To avoid a bias, the latter is predicted without using the information of the considered hit. In the barrel part of the tracker, the residuals in local x' and y' direction, parallel to u and v, will be shown. The sign is chosen such that positive values always point into the same $r\phi$ and z directions, irrespective of the orientation of the local coordinate system. For the wedge-shaped sensors as in TID and TEC, the residuals have a correlation depending on the local x- and y-coordinates of the track impact point. The residuals in global $r\phi$- and r-coordinates therefore are used for these modules.

In addition to misalignment, hit residual distributions depend on the intrinsic hit resolution and the track prediction uncertainty. For low-momentum tracks (as expected to dominate the TIF data) in the CMS tracker, the latter is large. For a momentum of 1 GeV/c and an extrapolation as between two adjacent TOB layers between two consecutive hits, the mean multiple scattering displacement is about 250 μm. So even with perfect alignment

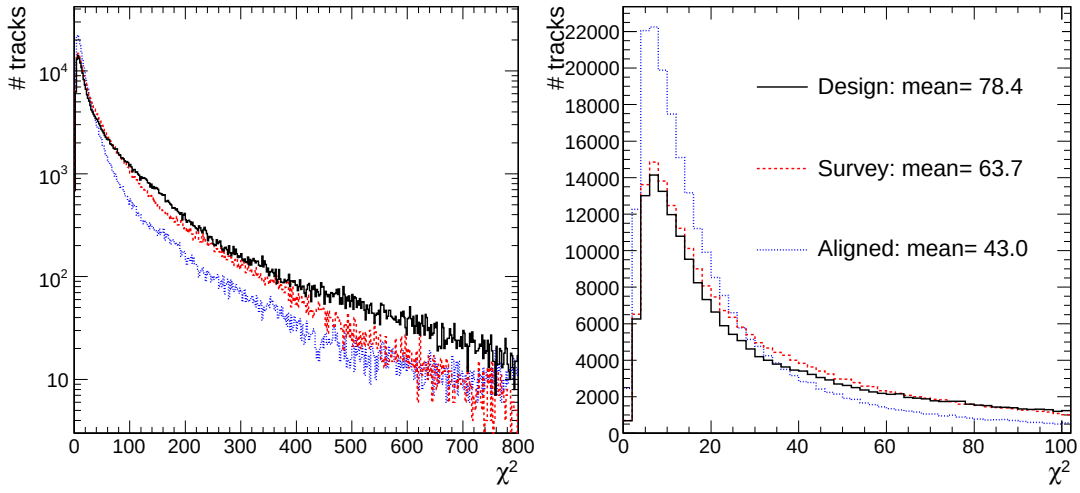

Figure 12: *Distributions of the absolute χ^2-values of the track fits for the design and survey geometries as well as the one from HIP track-based alignment.*

one expects a width of the residual distribution that is significantly larger than the intrinsic hit resolution of up to $23 - 53$ μm in the strip tracker barrel [2].

Another way of validating alignment results is provided by direct comparison of the obtained tracker geometries. This is done by showing differences between the same module coordinate in two geometries (e.g. ideal and aligned) vs. their geometrical position (e.g. r, ϕ or z) or correlating these differences as seen by two different alignment methods. Since not all alignment algorithms fix the position and orientation of the full tracker, comparison between two geometries is done after making the centre of gravity and the overall orientation of the considered modules coincide.

4.2 Validation of the Assembly and Survey Precision

Improvements of the absolute track fit χ^2 are observed when design geometry, survey measurements, and track-based alignment results are compared, as shown in Fig. 12. The average χ^2 changes from $78 \rightarrow 64 \rightarrow 43$ between the three geometries, respectively. This is also visible in the absolute hit residuals shown in Fig. 13. In general, an improvement can be observed by comparing the survey information to the design geometry, and comparing the track-based alignment to survey results. The residual mean values are closer to zero, and the standard deviations are smaller.

In Fig. 14, the differences of the module positions between the design geometry and the geometry aligned with the HIP algorithm are shown for TIB and TOB. There is a clear coherent movement of the four layers of the TIB in both radial (r) and azimuthal (ϕ) directions. The scale of the effect is rather large, $1 - 2$ mm. At the same time, mounting placement uncertainty of modules in TOB is much smaller for both layers within the TOB and for modules within layers. No obvious systematic deviations are observed apart from statistical scatter due to mounting precision.

Given good assembly precision of the TOB discussed above, the ideal geometry is a sufficiently good starting geometry for TOB. Therefore, only high-level structure survey is considered for TOB and no detailed comparison can be discussed. As a result, TOB residuals in Fig. 13 do not change much between survey and ideal geometries, the two differing only in the overall TOB global position as shown in Fig. 4.

However, the situation is different for TIB and optical survey is necessary to improve the initial understanding of the module positions in this detector. From Figs. 4 and 14 it is evident that survey of the layer positions in TIB does not reflect the situation in data (displacement appears to be even in the opposite direction). Therefore, we do not consider layer-level survey of TIB in our further analysis and do not include it in the track-based validation. However, the position of modules within a layer is reflected well in the optical survey. This is evident by significant improvement of the TIB residuals between the ideal and survey geometries shown in Fig. 13, and in the track χ^2 in Fig. 12.

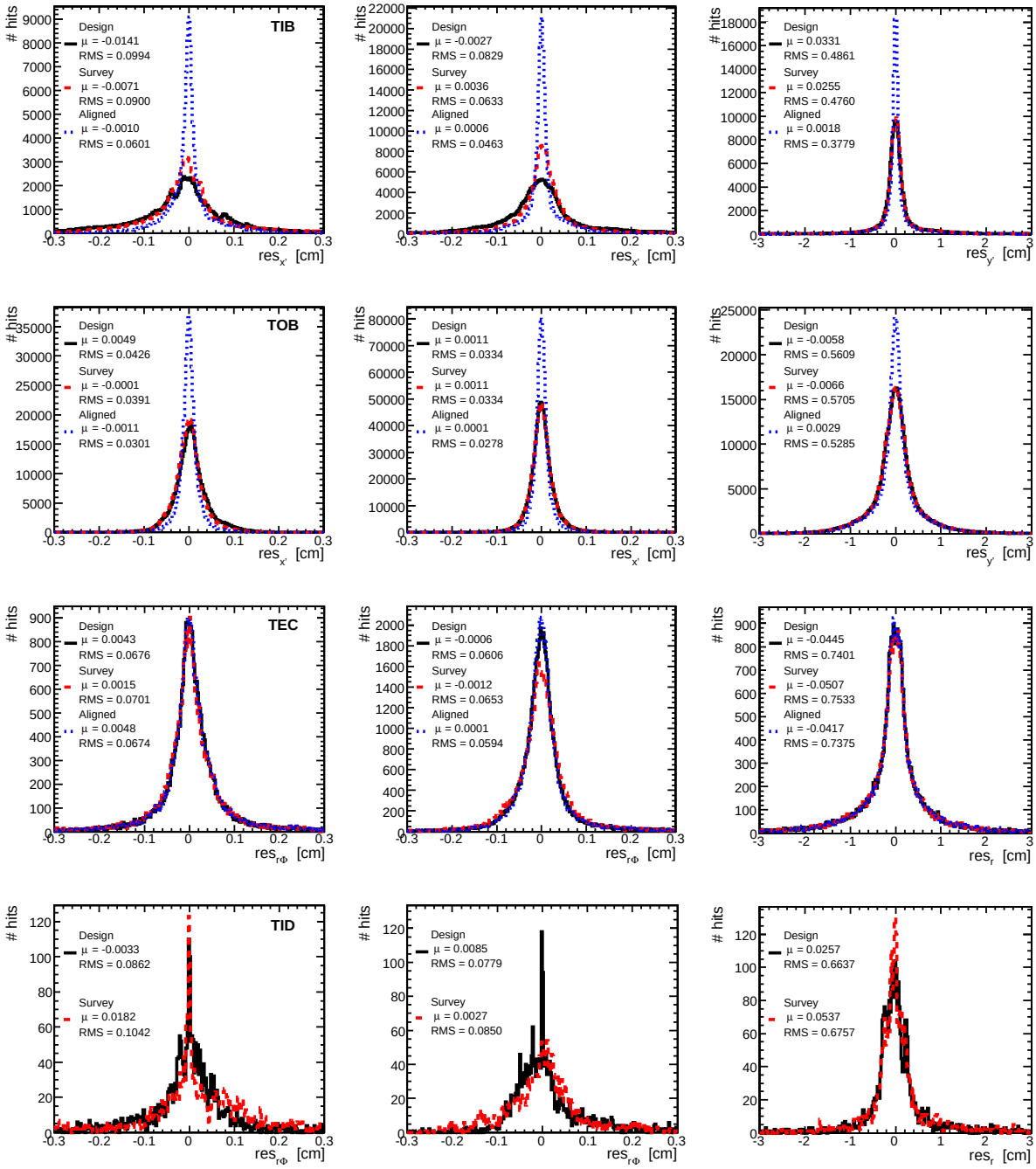

Figure 13: *Hit residuals for different geometries: ideal (solid/black), survey (dashed/red), and track-based alignment (dotted/blue, HIP). Four Tracker sub-detectors are shown in the top row (TIB), second row (TOB), third row (TEC), and bottom row (TID). The absolute local x'-residuals are shown for single-sided modules (left) and double-sided modules (middle), while local y'-residuals are shown for the double-sided modules only (right). For the endcap modules (in TEC and TID) transformation to the $r\phi$ and r residuals is made.*

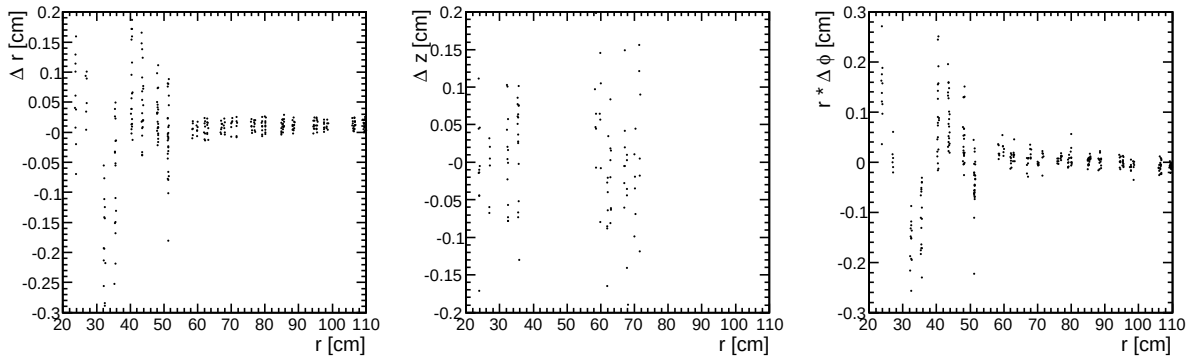

Figure 14: *Difference of the module positions between the measured (in HIP track-based alignment) and design geometries for TIB (radius $r < 55$ cm) and TOB ($r > 55$ cm). Projection on the r (left), z (middle), and ϕ (right) directions are shown. Only double-sided modules are considered in the z comparison.*

4.3 Validation of the Track-Based Alignment

The three track-based alignment algorithms used in this study employ somewhat different statistical methods to minimise hit residuals and overall track χ^2. Therefore, comparison of their results is an important validation of the systematic consistency of the methods.

To exclude the possibility of bad convergence of the track-based alignment, the alignment constants have been computed with random starting values. As an example, the starting values for the local shifts were drawn from a Gaussian distribution with a variance of $\sigma = 200$ μm. The corresponding results for the Kalman algorithm can be seen in Fig. 15, where in the upper two plots the computed global shifts for the sensitive coordinates are compared to ones from the standard approach. Also, starting from the survey geometry rather than the ideal geometry was attempted, as shown in the lower two plots. The results are compatible within their uncertainties as they are calculated inside the Kalman algorithm.

The three alignment algorithms show similar distributions of the track χ^2 shown in Fig. 16. HIP constants give the smallest mean value whereas Kalman and Millepede have more tracks at low χ^2 values than the HIP constants. The three algorithms also have consistent residuals in all Tracker sub-detectors as shown in Fig. 17, though the most relevant comparison is in the barrel region (TIB and TOB) since the endcaps were not aligned at the module level. For both Figs. 16 and 17, only modules selected for alignment have been taken into account in the refit and in the residual distributions.

A more quantitative view of the residual distributions and their improvement with alignment can be gained by looking at their widths. To avoid influence of modules not selected for alignment in the following, these are excluded from the residual distributions and from the track refits. Furthermore, taking the pure RMS of the distributions gives a high weight to outliers e.g. from wrong hit assignments in data or artificially large misaligned modules in simulations (see Sec. 4.5). For this reason truncated mean and RMS values are calculated from the central 99.87% interval of each distribution, corresponding to 2.5σ for a Gaussian-distributed variable. The resulting widths of the residual distributions in x' after alignment (HIP constants) are shown in Fig. 18 for the ten barrel layers. They are about 120 μm in TOB layers 2-5, between 200 and 300 μm in TIB layers 2-3 and much larger in TIB layer 1 and TOB layer 6. This is due to the much larger track pointing uncertainty if the track prediction is an extrapolation to the first and last hit of a track compared to interpolations for the hits in between, as can be seen from the second curve in Fig. 18. Here residuals from the first and last hits of the tracks are not considered. Residual widths in TIB decrease clearly to about 150 μm, making it evident that many tracks end within the TIB. TIB layer 1 and TOB layer 6 now show especially small values since all remaining residuals come from sensor overlap and have short track interpolation distances.

The truncated mean and RMS values of these residual distributions are shown in Fig. 19 for the HIP alignment result compared to the results before alignment, showing clearly the improvements. The mean values are now close to zero and the RMS decreases by at least almost a factor of two.

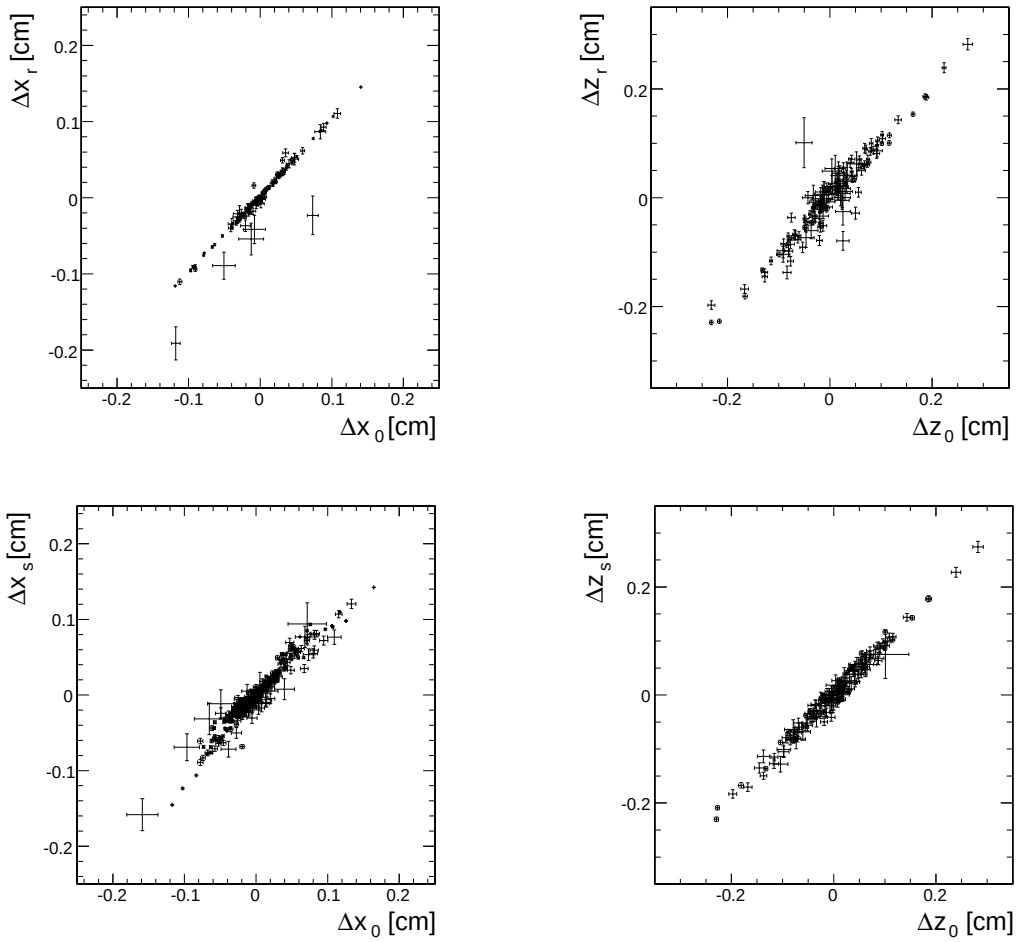

Figure 15: Comparison of the global shifts computed with different starting values, using the Kalman alignment algorithm. For the computation of Δx_0 and Δz_0 the starting values for parameters were set to 0, for Δx_r and Δz_r they were drawn from a Gaussian distribution and for ΔX_S and ΔZ_S they are taken from the module survey geometry.

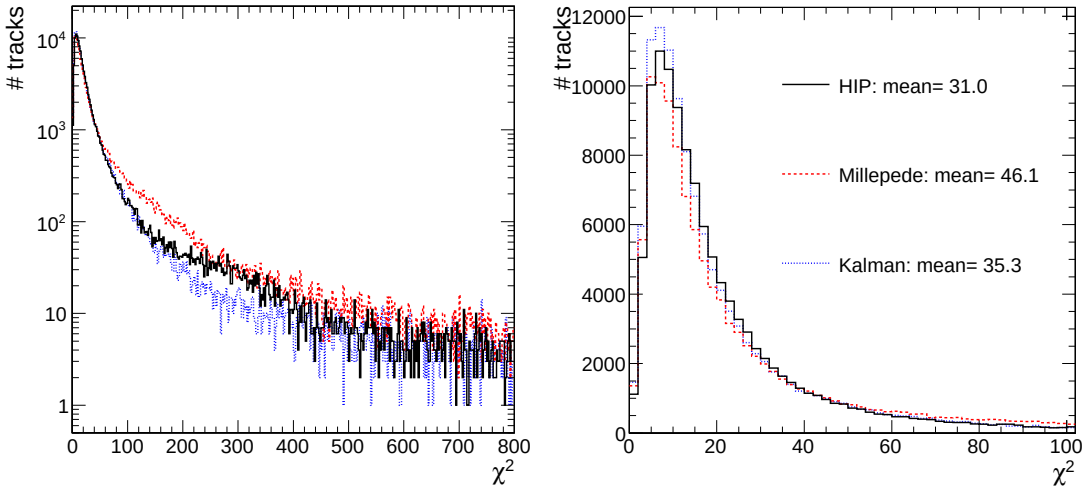

Figure 16: *Distributions of the absolute χ^2-values of the track fits for the geometries resulting from HIP, Kalman, and Millepede alignment. The track fit is restricted to modules aligned by all three algorithms.*

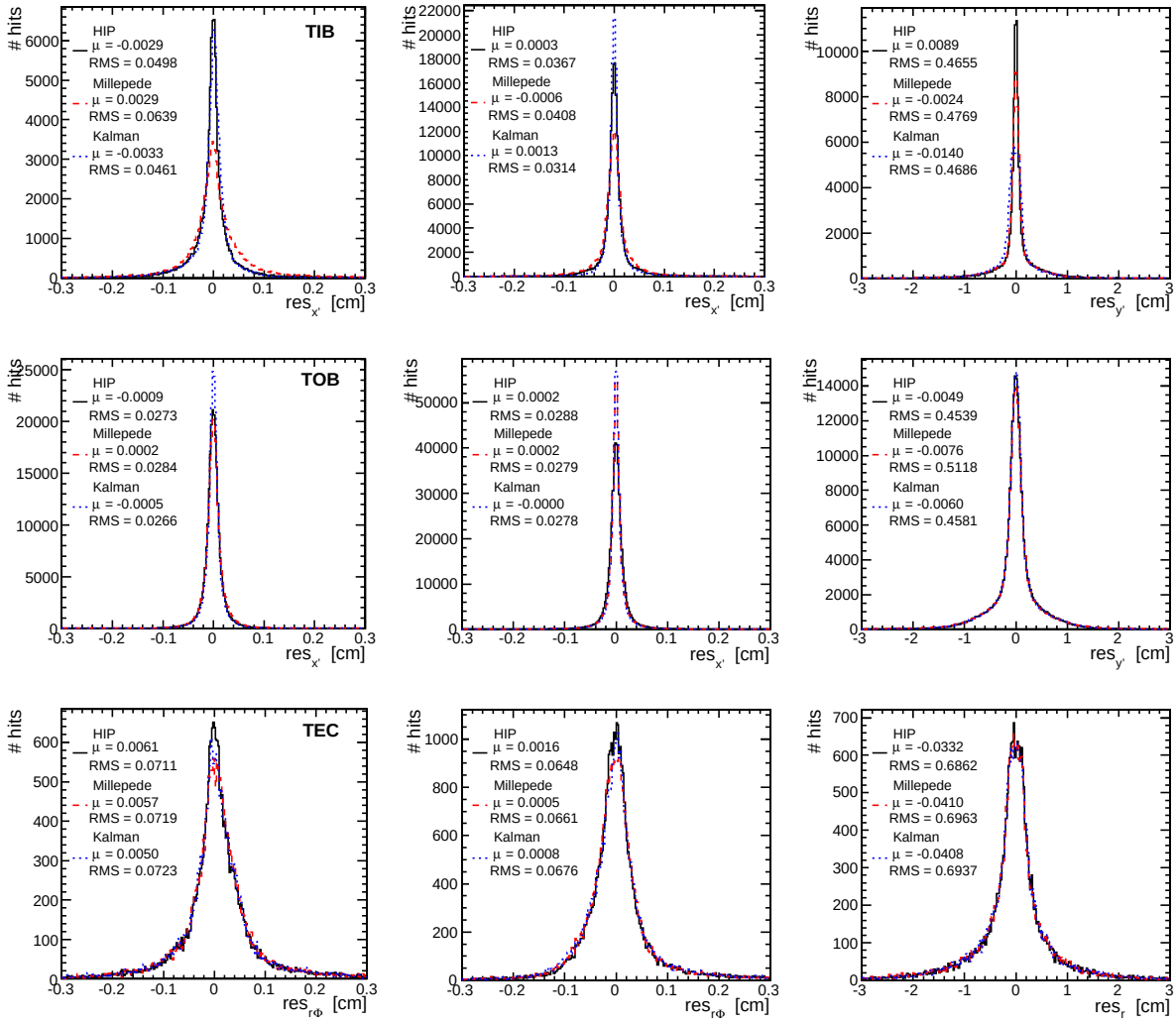

Figure 17: *Hit residuals for different geometries from three track-based algorithms: HIP (solid/black), Millepede (dashed/red), and Kalman (dotted/blue) based alignment. Three Tracker sub-detectors are shown in the top row (TIB), second row (TOB), and bottom row (TEC). The absolute local x'-residuals are shown for single-sided modules (left) and double-sided modules (middle), while local y'-residuals are shown for the double-sided modules only (right). For the endcap modules (TEC) transformation to the $r\phi$ and r residuals is made. The track fit is restricted to modules aligned by all three algorithms.*

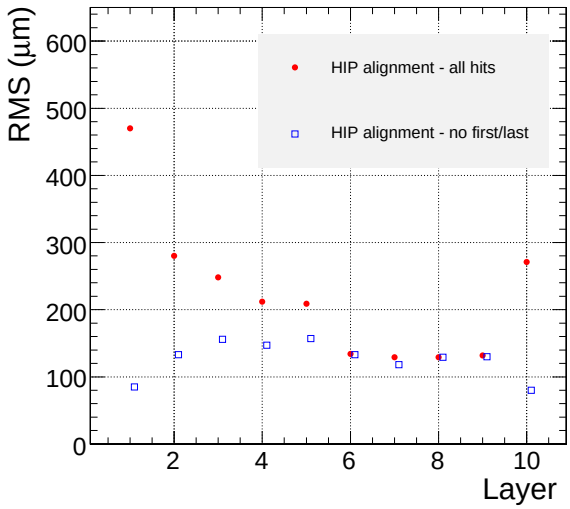

Figure 18: *Hit residual RMS in local x' coordinate in ten layers of the barrel tracker, i.e. four layers of TIB and six layers of TOB, after track-based alignment with HIP. In contrast to the red circles, the blue squares are obtained including residuals from the first and last hits of the track. Hits on modules not aligned are not considered in the track fit.*

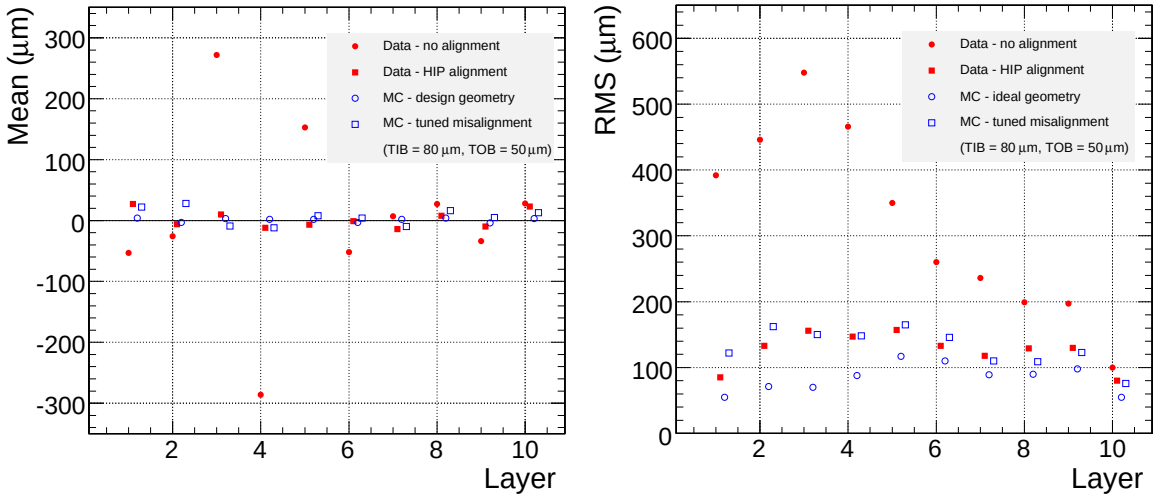

Figure 19: *Hit residual means in local x' coordinate (left) and RMS (right) in ten layers of the barrel tracker, i.e. four layers of TIB and six layers of TOB, shown in data before track-based alignment (red full circles), after track-based alignment (HIP, red full squares), in simulation with ideal geometry (blue open circles) and in simulation after tuning of misalignment according to data (blue open squares).*

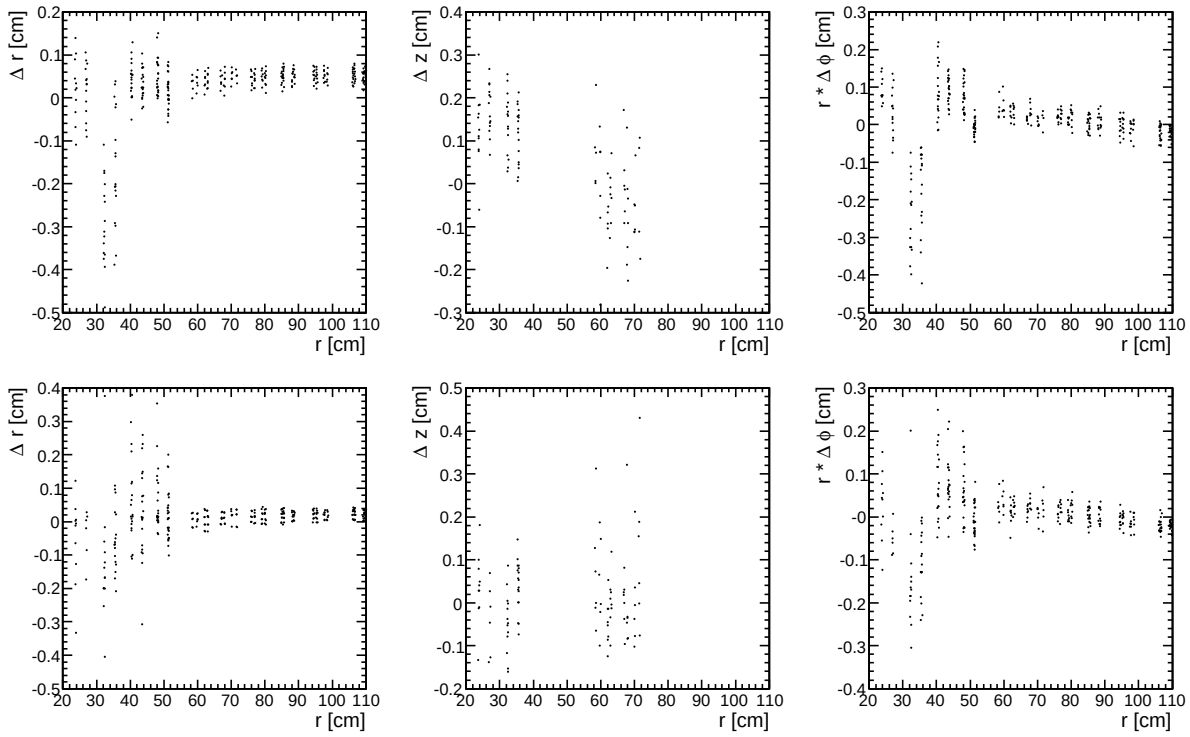

Figure 20: *Difference of the module positions between the measured (in track-based alignment) and design geometries shown for Kalman (top) and Millepede (bottom) algorithms for TIB (radius $r < 55$ cm) and TOB ($r > 55$ cm). Projection on the r (left), z (middle), and ϕ (right) directions are shown. Only double-sided modules are considered in the z comparison.*

4.4 Geometry comparisons

Overall, a very consistent picture is observed when the same comparison to design geometry, as shown in Fig. 14 for the HIP constants, is done with the other two algorithms in Fig. 20. In all cases, the same coherent movement of TIB layers is found, while TOB mounting precision is consistently better.

Consistency of the three algorithms is shown in Fig. 21 where the $r\phi$, z, r, x and y differences from ideal geometry of the result of the three algorithms is compared to each other. A good correlation of the results is observed, especially in the x displacement, which is the most sensitive coordinate with vertical tracks. The main residual deviation from the diagonal 100% correlation is due to statistical and systematic differences in the approaches, therefore reflecting the achieved precision of the methods. The numerical results of comparison of different geometries are shown in Table 2. The RMS of agreement between algorithms in the x coordinate is as good as 150 μm, except for comparison of the Millepede constants in the TIB.

As discussed in Sec. 3.2, no attempt to align the TID was made and for the TEC, only rotation of the nine disks around the global z coordinate was studied, due to limited track statistics in the endcaps. Comparison of the resulting geometry in two algorithms (HIP and Kalman) is shown in Fig. 22. The results exhibit slight differences, but they clearly show the same trend.

4.5 Track-Based Alignment with Simulated Data and Estimation of Alignment Precision

Alignment tests on simulated data have been performed with the Kalman algorithm on approximately 40k events from a sample that mimics the situation at the TIF. In order to reproduce our knowledge of the real tracker geometry after survey measurements only, movements and errors to the tracker elements are applied according to the expected starting misalignment [12]. The alignment strategy and track selection discussed above are applied to obtain the results shown in Fig. 23, resulting in a precision of 80 μm in global x position.

An alignment study on the full MC data set has been performed with the Millepede algorithm with the same settings as for the data, i.e. alignment of a subset of the barrel part at module level and of the TEC at disk level. The resulting residual distributions in TIB, TOB and TEC are shown in Fig. 24 and compared with the startup

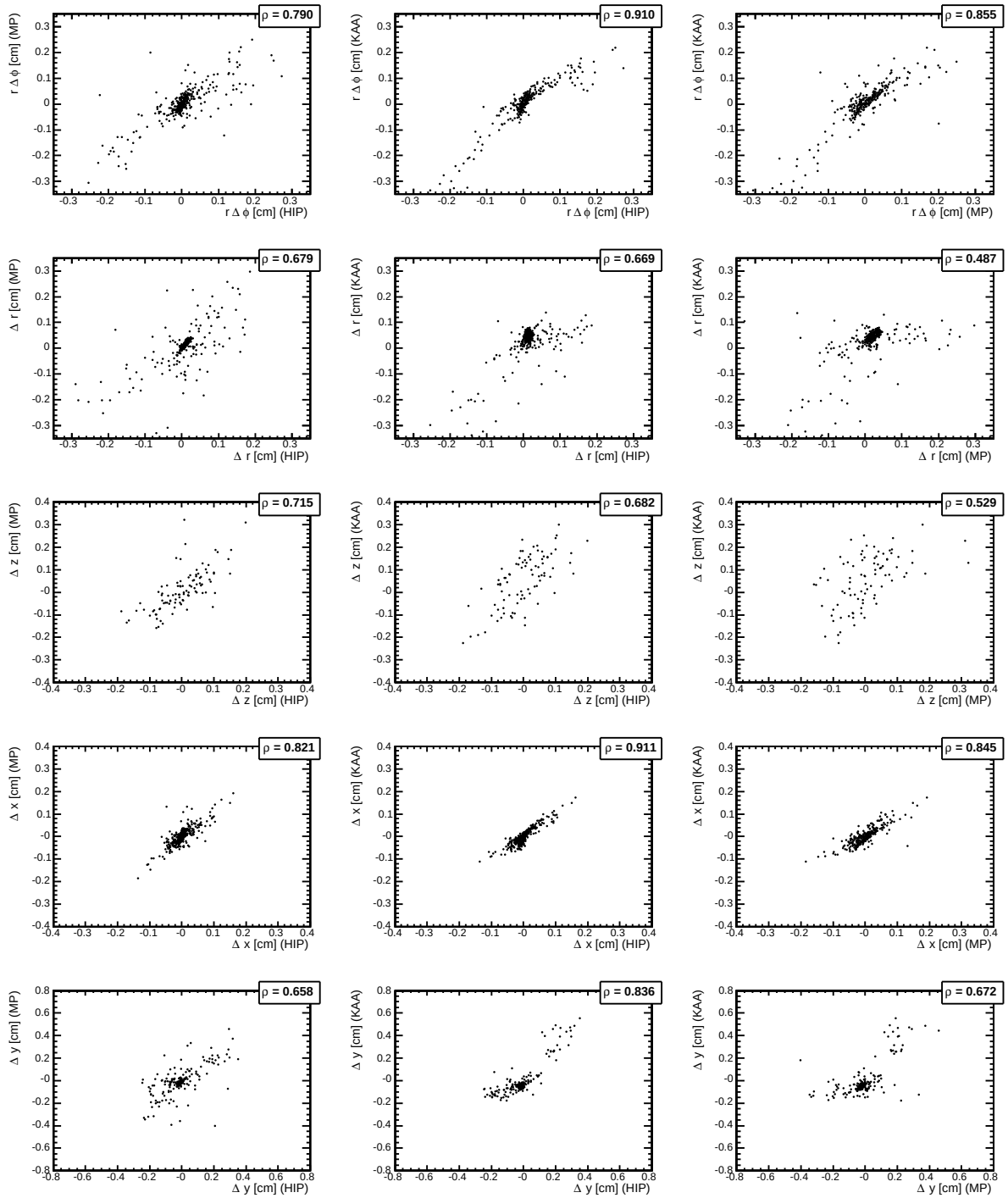

Figure 21: *Direct comparison of differences from ideal geometry in $r\phi$ (top), z (second row), r (third row), x (fourth row), and y (bottom) between Millepede and HIP (left), Kalman and HIP (middle), and Kalman and Millepede (right). The correlation coefficient ρ is stated.*

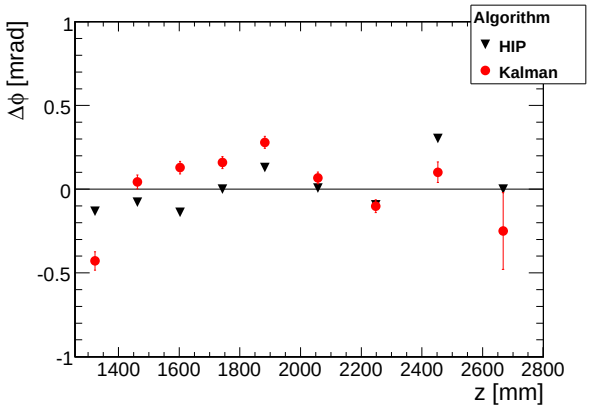

Figure 22: *Rotations of the TEC disks around the global z in comparison of the measured (in track-based alignment) and design geometries for TEC. Two track-based results are shown: HIP (triangles) and Kalman filter (circles) algorithms.*

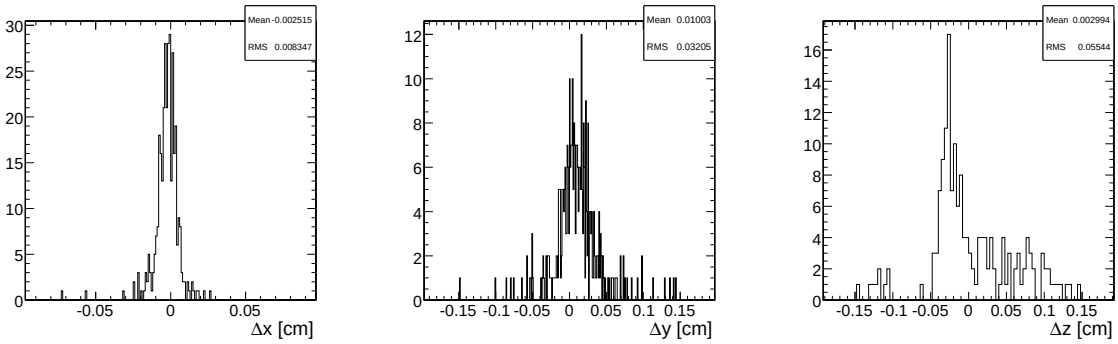

Figure 23: Alignment resolution in global coordinates achieved with the Kalman alignment algorithm on simulated data.

Table 2: *Comparison of the global x, y and z RMS difference (in μm) of module positions between different geometries indicated in the first two columns for TOB and TIB. Single-sided (SS) and double-sided (DS) modules are shown together and separately.*

Geom 1	Geom 2	difference	TIB	TIB (SS)	TIB (DS)	TOB	TOB (SS)	TOB (DS)
HIP	Design	Δz	-	-	638	-	-	806
MP	Design	Δz	-	-	787	-	-	1139
KAA	Design	Δz	-	-	706	-	-	1053
KAA	HIP	Δz	-	-	429	-	-	487
MP	HIP	Δz	-	-	533	-	-	805
KAA	MP	Δz	-	-	698	-	-	614
HIP	Design	Δx	526	438	581	130	108	142
MP	Design	Δx	623	500	653	236	206	208
KAA	Design	Δx	543	500	519	237	215	173
KAA	HIP	Δx	165	138	193	159	156	74
MP	HIP	Δx	341	297	383	162	148	151
KAA	MP	Δx	304	226	396	123	132	97
HIP	Design	Δy	1353	914	1639	93	88	103
MP	Design	Δy	1527	1173	1488	144	125	183
KAA	Design	Δy	1751	541	2180	141	132	164
KAA	HIP	Δy	850	471	1036	94	80	123
MP	HIP	Δy	1202	1043	1417	101	80	139
KAA	MP	Δy	1324	842	1845	59	57	63

misalignment [12] and the ideal geometry. Comparison with the distributions obtained from data using the design geometry (Fig. 17) reveals that in TIB and TOB the starting misalignment is overestimated while in TEC it is slightly underestimated. The residual widths after alignment are generally much smaller than those obtained from the aligned data, especially in the TIB. This could be due to the larger statistics of the simulation data sample, but also due to effects not properly simulated, e.g. relative misalignment of the two components of a double-sided module or possible differences in the momentum spectrum of Monte Carlo.

The results of the truncated RMS of the layerwise residual distributions in Fig. 19 are used to estimate alignment precision in the aligned barrel region via comparison with simulations. Different misalignment scenarios have been applied to the ideal ("true") Tracker geometry used in reconstructing the simulated data until truncated RMS values are found to be similar to the ones in data in all layers. The modules in TIB and TOB have been randomly shifted in three dimensions by Gaussian distributions. The influence of possibly large misalignments from the tails of these Gaussians is reduced by truncating the distributions as stated above.

Besides the truncated mean and RMS values from data before and after alignment, Fig. 19 shows also the results from the simulation reconstructed with the ideal geometry and reconstructed with a random misalignment according to Gaussian distributions with standard deviations of 50 μm and 80 μm in the TOB and the TIB, respectively. It can be clearly seen that the simulation with the ideal, i.e. true, geometry has smaller widths than the data, especially in the TIB. On the other hand, the geometry with a simulated misalignment of 50 μm and 80 μm, respectively, resembles rather well the data after alignment, such that these numbers can well be taken as an estimate of the size of the remaining misalignment.

5 Stability of the Tracker Geometry with Temperature and Time

5.1 Stability of the Tracker Barrels

In order to investigate stability of the tracker components with respect to the cooling temperature and stress due to TEC insertion, full alignment of the Tracker in different periods has been performed and the positions of modules in space are compared. The advantage of this approach is that we can see module movements directly, but the potential problem is that we may be misled by a systematic effect or a weakly constrained misalignment. Statistical scatter of up to 100 μm limits the resolution of the method. These tests have been done with the HIP algorithm.

1. **+15 °C (A_1, before TEC- insertion) vs. +10 °C (C_{10}, after TEC- insertion).**

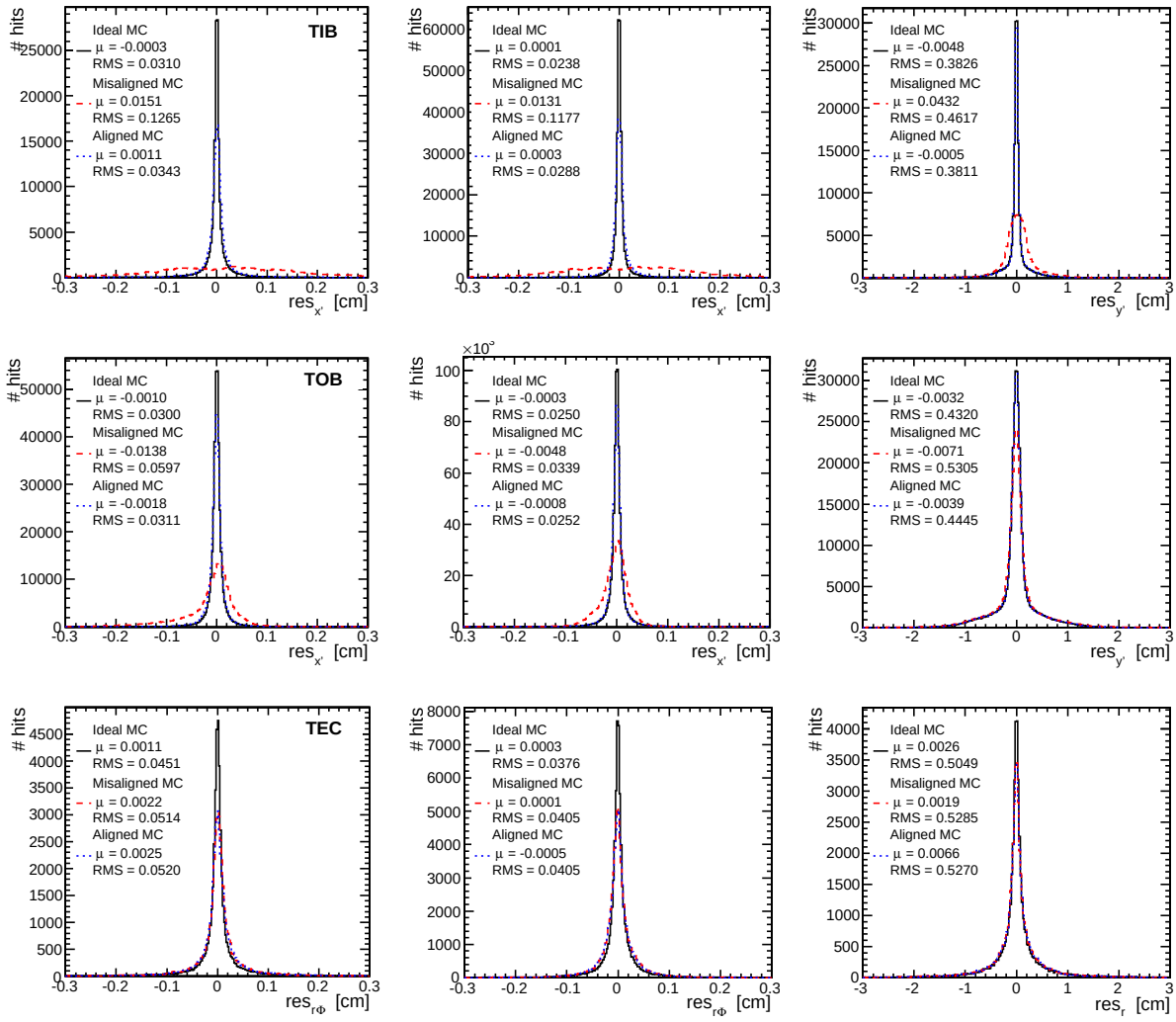

Figure 24: *Hit residuals for different geometries in different conditions for the simulated data sample: ideal geometry (solid/black), misaligned geometry according to expected starting misalignment (dashed/red), and geometry after alignment (dotted/blue). Three Tracker sub-detectors are shown in the top row (TIB), second row (TOB), and bottom row (TEC). The absolute local x-residuals are shown for single-sided modules (left) and double-sided modules (middle), while local y-residuals are shown for the double-sided modules only (right). For the endcap modules (TEC) transformation to the $r\phi$ and r residuals is made.*

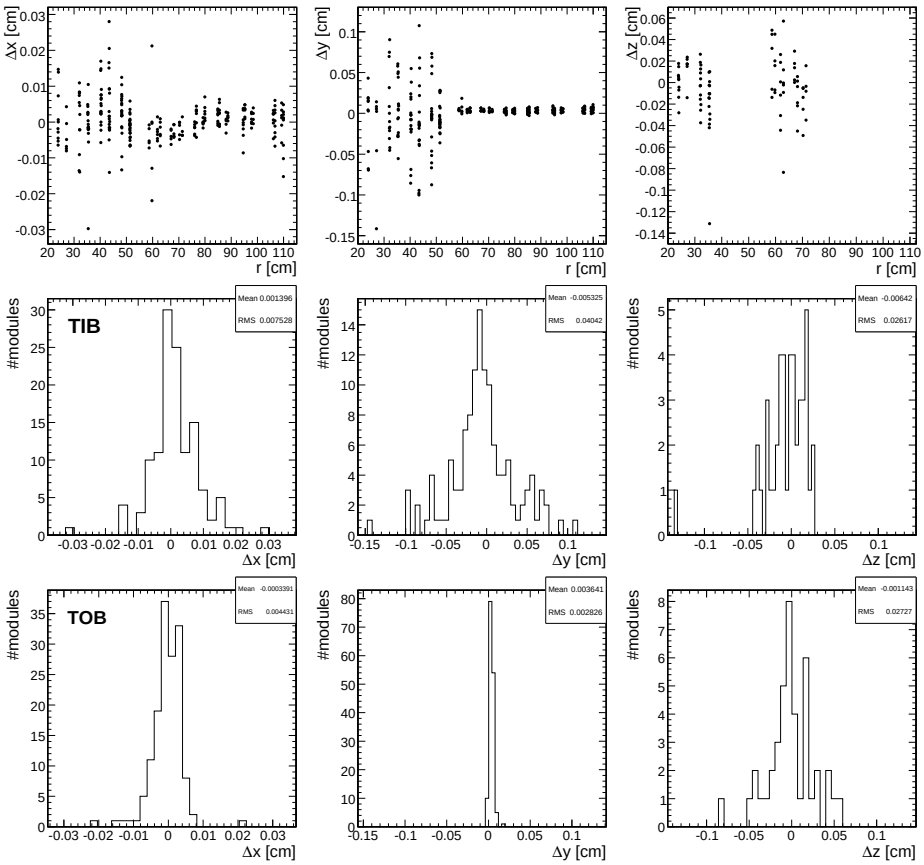

Figure 25: *Differences in determined x- (left), y- (centre) and z-positions (right, only double-sided) of active modules comparing the configurations before and after TEC- insertion. The differences are stated as a function of the module radius r (top row) and for modules in TIB (middle row) and TOB (bottom row) separately.*

This test is intended to show the effect of the insertion of a mechanical object between two data-taking conditions. Fig. 25 shows the shifts between the two sets of aligned positions in global x, y and z as a function of the radial coordinate and projected separately for TIB and TOB.

In the TOB, a very small layer-wise shift is visible, especially in layers one and two.

As can be seen from Fig. 26, there is no further structure as a function of the z coordinate. This could be a hint of a small layer-wise rotation around the z axis. In the TIB, coherent movements are larger in the azimuthal direction and are also layer-dependent; but here, they are reflected in the corresponding structures in the longitudinal direction: the movement is largest closer to $z = 0$ and is reduced to small values at large z (see Fig. 26). We interpret it as a layer- and side-dependent twist where the outer edges in z are better constrained due to the mechanical mounting technique. However, it is also possible that there is not enough information to constrain the "weak" degrees of freedom, or this could be an artificial effect due to different modules being aligned in different configurations and different track samples due to different trigger configurations.

2. **-10 °C (C_{-10}, default sample) vs. +10 °C (C_{10}).**

   This test is intended to show the effect of a large temperature gap between two data-taking conditions. Figure 27 shows the shifts between the two sets of aligned positions in global x, y and z as a function of the radial coordinate and projected separately for TIB and TOB.

   All deviations are within what appears to be statistical scatter, so this comparison does not show statistically significant movements. In the TOB, though certain layers exhibit larger scatter than the others, there is no evidence of any coherent shift. In the TIB, there are hints of a small systematic shift vs. the layer number increasing towards outer layers, that could be caused by a relative movement between the cylinders or a rotation around the global z axis. No dependence vs. global z is observed, excluding large effects of a

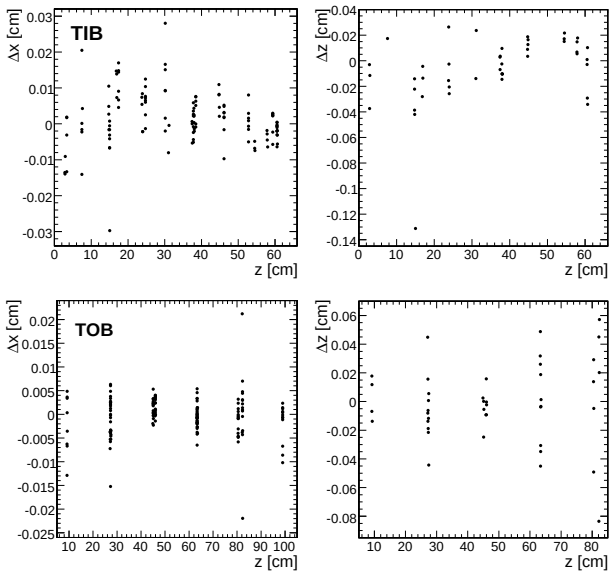

Figure 26: *Differences in determined x- (left) and z-positions (right, only double-sided) of active modules comparing the configurations before and after TEC- insertion as a function of the module r-position for modules in TIB (upper row) and TOB (bottom row).*

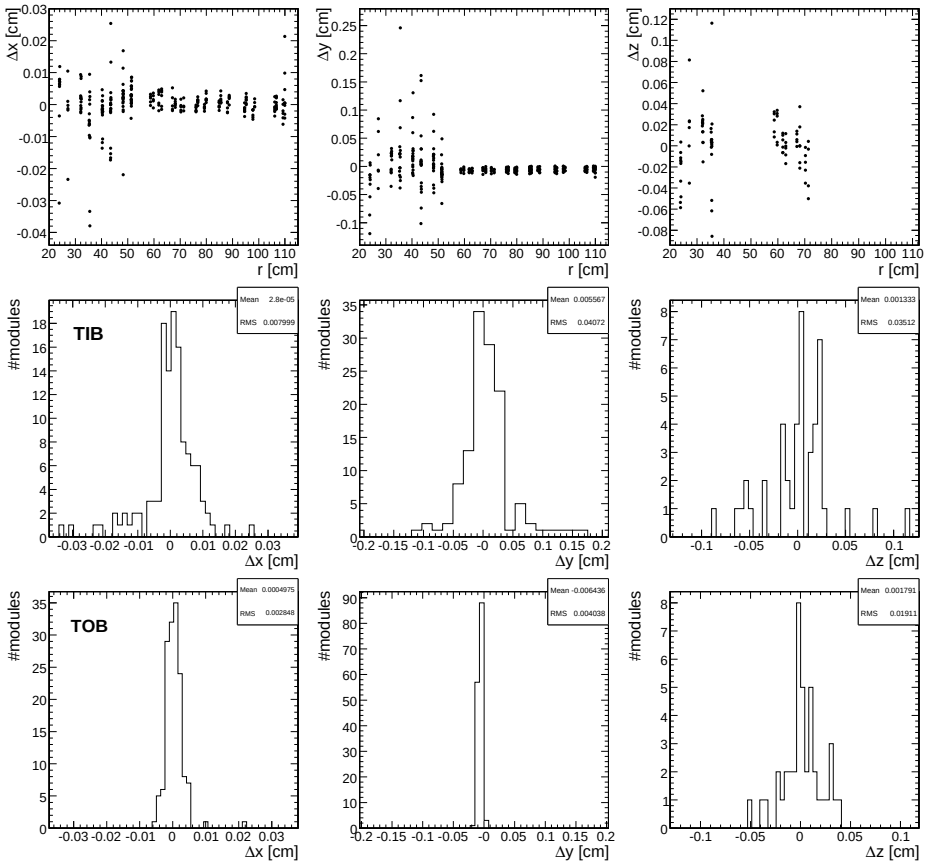

Figure 27: *Differences in determined x- (left), y- (centre) and z-positions (right, only double-sided) of active modules comparing the +10 °C and -10 °C configurations. The differences are stated as a function of the module radius r (top row) and for modules in TIB (middle row) and TOB (bottom row) separately.*

rotation about the y direction or a twist.

5.2 Stability of the Tracker Endcap

For the TEC stability validation, a comparison is made of the disk alignment with tracks, using the Kalman filter algorithm, for the temperature levels: room temperature, 10 °C, -1 °C, -10 °C, -15 °C, and 14 °C. The alignment parameters calculated with these data sets are shown on the left of Fig. 28. The determined alignment parameters for the different tracker temperatures agree with each other within their errors. Disk nine is never hit in the data taken at -15 °C or 14 °C; therefore, there are only eight alignment parameters available at these temperature levels. At -15 °C, the experiment setup changed: Only the back petals have been activated because there was not enough cooling power.

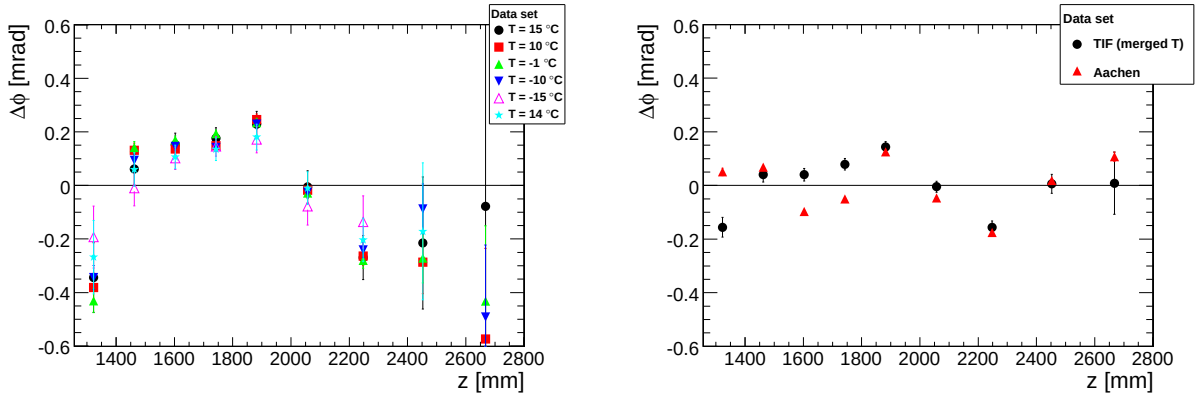

Figure 28: *Alignment parameter $\Delta\phi$ for TEC disks at six tracker temperature levels (left). Alignment parameter $\Delta\phi$ for TEC disks, determined with TIF data and Aachen data using an obsolete, but common geometry (right).*

In addition, during the TEC integration in Aachen, tracks from cosmic muons have been recorded. Here, the TEC had been positioned vertically. For each sector, data had been taken separately after its integration. The processing of these data had been done using a now obsolete geometry description. The modules on TEC rings 2 and 5 are displaced in this geometry by up to 140 μm.

To create equivalent results, an alignment in $\Delta\phi$ is determined with tracks from TIF data and compared with results from tracks of sector 2 and 3 of the data from Aachen. To avoid major differences in the alignment results due to changes in the geometry, the tracks of the TIF data are reconstructed using the same geometry as used for Aachen data. The right of Fig. 28 shows the alignment parameters gained from TIF and Aachen data. Except for some changes in disks 1, 3, and 4 of the order of 0.2 mrad, the TEC seems to have been stable during transportation from Aachen to Geneva, tilting from a vertical to a horizontal position, and integration into the tracker. Two petals have been replaced in the active TEC sectors before taking the TIF data: A back petal of disk 3 and a front petal of disk 4. Thus, changes in the corrections $\Delta\phi$ of these disks are expected.

6 Laser Alignment System Analysis and Discussion

In this section, we discuss results from the Laser Alignment System. Analysis of the measurements from this system have not been integrated with the track-based statistical methods. Therefore, we discuss the data analysis and results independently.

6.1 Data Taking

At the TIF, data was taken with the laser alignment system. On the z^+ side of the tracker, the beams from the alignment tubes of sector 1, 2 and 3 were seen by the barrel modules. The endcap sectors 2 and 3 were operated with the TEC internal beams and the alignment tubes of those sectors. Data was taken before cooling the tracker down, during the cooling cycle, and at the end, when the tracker was back at room temperature.

As we mentioned earlier, the Laser Alignment System was designed to measure deformations and movements of the tracker support structures. To do this properly, the whole ϕ-range of the laser beams needs to be operated. The fact that only a slice of the tracker was operated during the TIF tests means that no complete picture of the tracker alignment parameters could be obtained. Nevertheless, the data taking was very useful to verify the proper

functioning of the laser beams and the laser data taking. First of all, the evolution of the measured laser spot positions with temperature was studied. Movements could be either due to thermal deformations of the tracker structure, or caused by small movements of the beamsplitter holders. Then, the data taken in the TEC sectors can be compared to the data obtained during the TEC integration. Here, observed differences could also have been caused by the handling, transport and insertion of the endcaps.

6.2 Results from Alignment Tubes

The alignment tubes were first operated at room temperature. Then, as the tracker was gradually cooled down, they were measured at 10 °C, -1 °C, -15 °C and finally again at room temperature, after the tracker had been warmed up again. The measured laser spot positions were all compared to the first measurements at room temperature. The result is shown in Fig. 29. The largest changes of about 600 μm were observed in the TOB. The observed movements could come either from movements of the tracker structure, or from movements of the laser beams. Nevertheless, two bounds can be given. First, one could assume that all detected movements were due to tracker structure deformations. In this case, we would have observed movements of 600 μm. On the other hand, one could try to absorb as much as of the observed laser spot changes into movements of the laser beams. In this case, one calculates the tilt of the laser beams and rotations of the alignment tubes that fit best to the observed laser spot movements. After subtracting this contribution, the remaining laser spot movements would be due to the tracker support deformation. This is shown in Fig. 30. Now the maximal movements of the tracker would be less than 100 μm.

6.3 Comparison of LAS and Track Based Alignment Results

A comparison is made between the Laser Alignment System residuals and the TEC disk alignment results using track based alignment at different temperatures. Corrections are applied to the residuals because the beam splitters used by the LAS are known to emit two non-perfectly parallel laser beams. Considering the laser beamspot radii, the residuals measured at room temperature are transformed into disk rotations. The disc corrections, $\Delta\phi$, estimated with the Kalman alignment algorithm from cosmic track data are used for comparison. There are no significant changes in the TEC alignment evaluated with track based alignment at different temperatures, so the track data merged from all temperature runs except $T = -15$ °C were used to obtain a better precision.

Because the exact direction of the laser beams is unknown, a linear dependence of ϕ on z cannot be determined using the LAS residuals. Therefore, mean and slope (as a function of z) of the corrections to the disc rotations are subtracted. The same is done with the results from the Kalman alignment algorithm to use a common coordinate system. The remaining corrections are displayed in Fig. 31. For LAS, the mean and RMS of the four measurements estimated from the four active laser beams in the endcap are shown for each disk. There are differences among the LAS corrections for the same disk of up to 0.7 mrad. These differences are interpreted as misalignment on module and petal level. Considering the accuracy of the Kalman alignment parameters and the spread of the LAS results, the estimated corrections show a good agreement.

7 Summary and Conclusion

We have presented results of the CMS tracker alignment analysis at the Integration Facility at CERN by means of cosmic tracks, optical survey information, and the Laser Alignment System. The first alignment of the active silicon modules with three different statistical approaches was performed, using cosmic track events collected with the partially active CMS tracker during spring and summer of 2007.

Optical survey measurements of the tracker were validated with the track residuals in the active part of the detector. Clear improvement with respect to the design geometry description was seen. Overall, further significant improvements in track χ^2 and track-hit residuals are achieved after track-based alignment of the tracker at TIF, when compared either to design or survey geometry.

Detailed studies have been performed on the Tracker Inner and Outer Barrel alignment with tracks. The typical achieved precision on module position measurement in the local x coordinate is estimated to be about 50 μm and 80 μm in the Tracker Outer and Inner Barrels, respectively. However, since no magnetic field was applied in the tracker, no momentum estimate of the cosmic tracks was possible. Therefore, detailed understanding of alignment precision suffers from uncertainties in multiple scattering of tracks with unknown momentum, this being the dominant contribution to the hit resolution. For this reason, the above alignment precision estimates are based on prediction from simulations of hit residuals and may overestimate the detector misalignment.

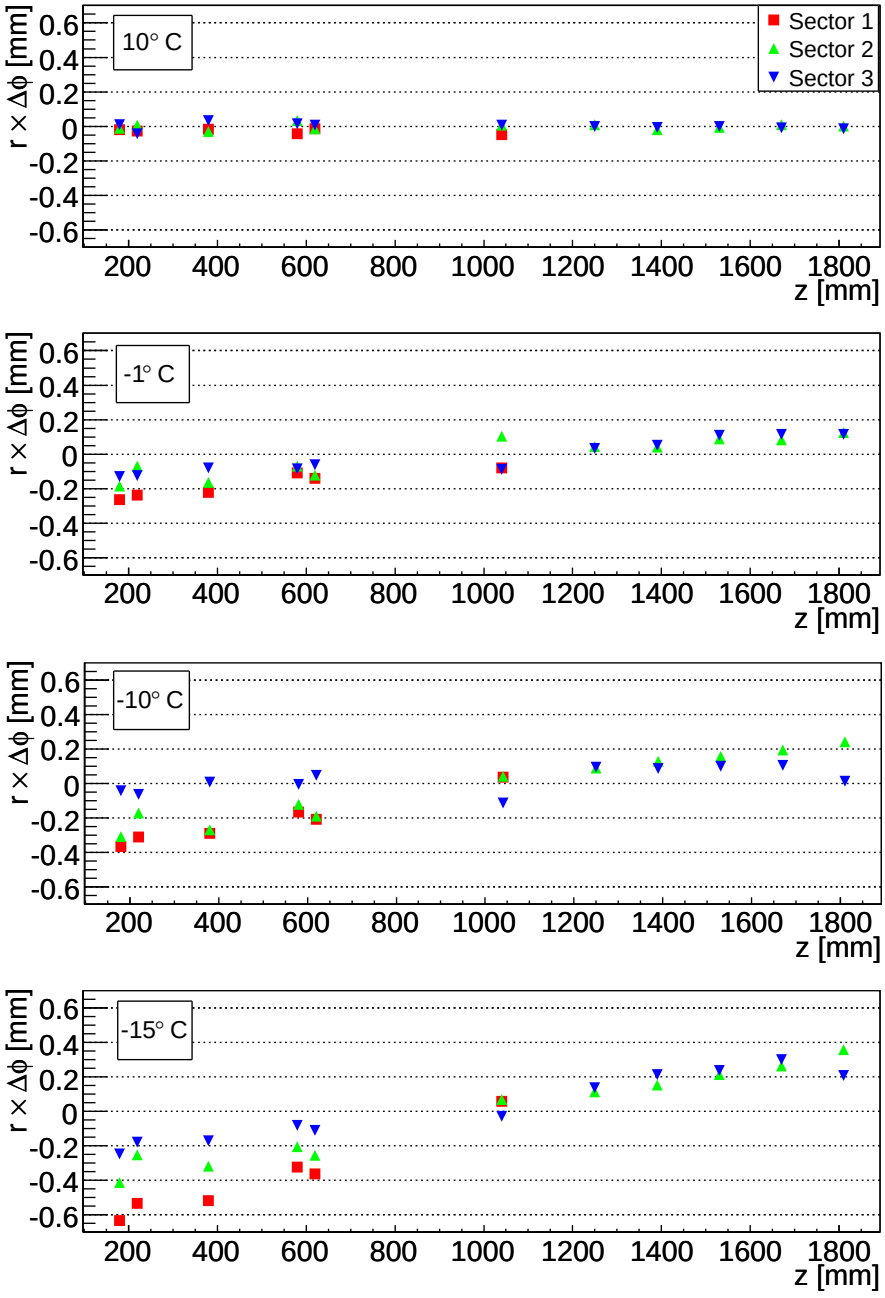

Figure 29: Changes in laser spot positions while cooling down the tracker.

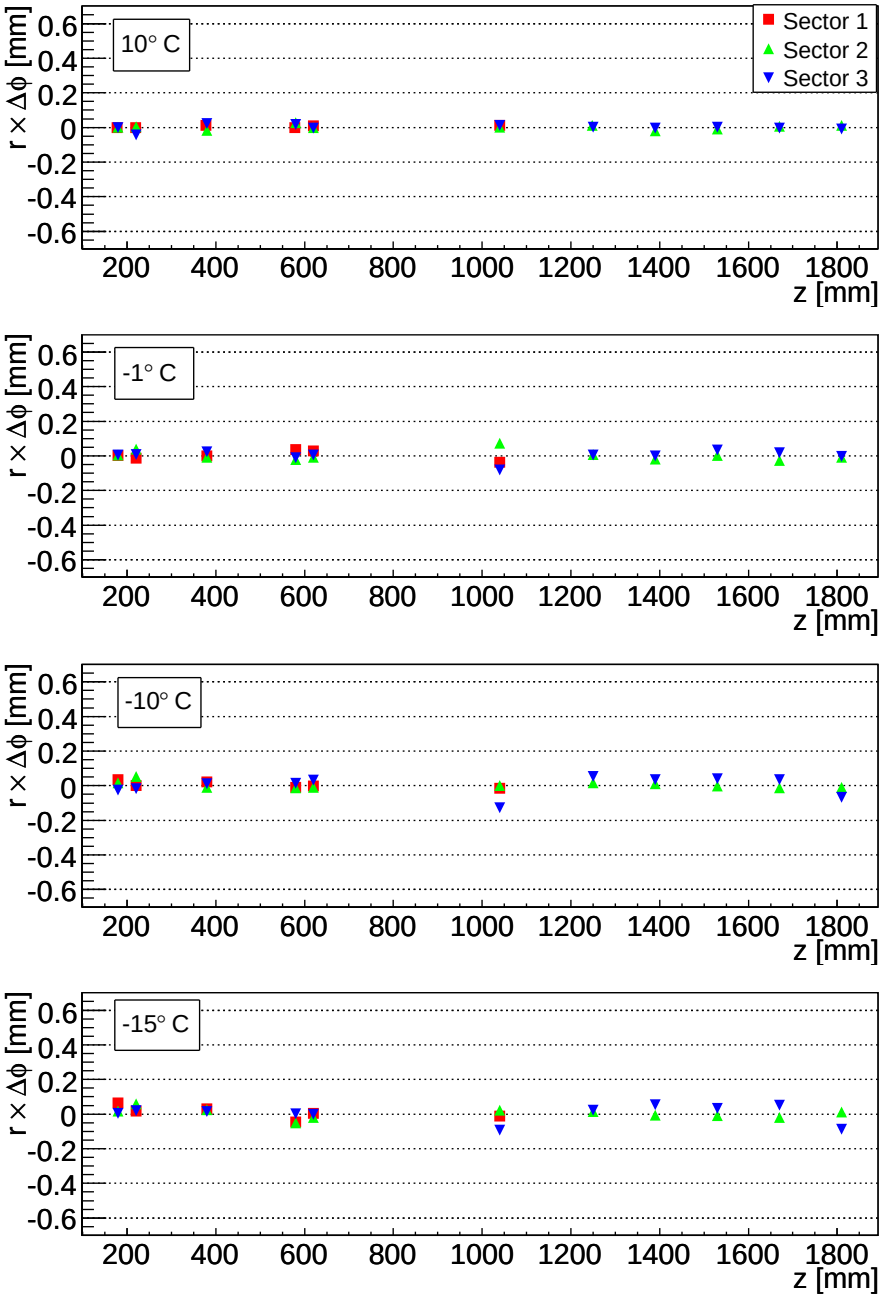

Figure 30: Changes in laser spot positions while cooling down the tracker, removing the maximum contribution that can be due to movements of the alignment tube.

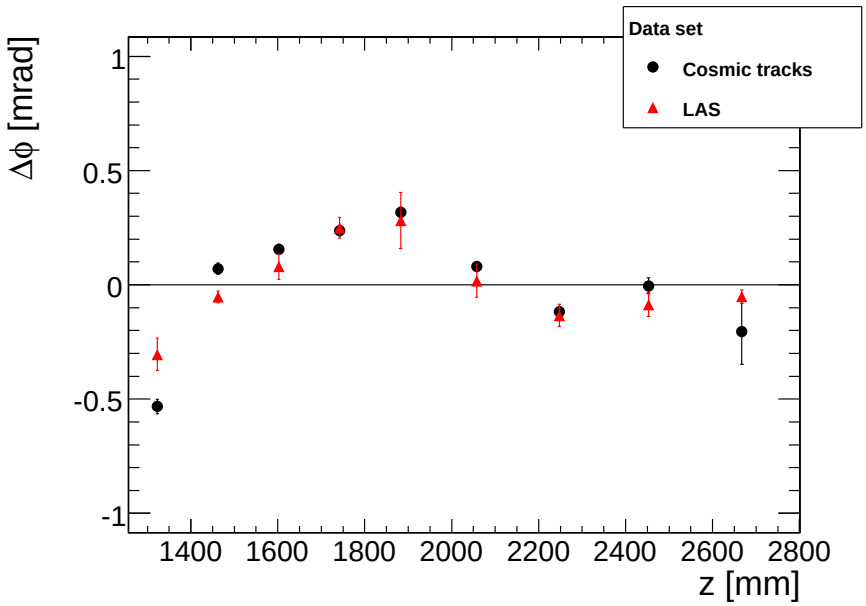

Figure 31: *Corrections $\Delta\phi$ for TEC disks determined with track based alignment and LAS residuals.*

Consistent alignment results have been obtained with three different alignment algorithms Direct comparison of obtained geometries indicate $\sim$150 μm consistency in the precisely measured coordinate, consistent with the indirect interpretation of track residuals. However, certain χ^2-invariant deformations appear in the alignment procedure when using only cosmic tracks. These χ^2-invariant deformations do not affect track residuals and therefore are not visible in the alignment minimisation, thus limiting understanding of relative position of all modules in space from the pure geometrical point of view.

Alignment of the Tracker Endcap was performed at the disk level, both with tracks and by operating the CMS Laser Alignment System and showed good agreement between the two results.

No significant deformations of the tracker have been observed under stress and with variation of temperature, within the resolution of the alignment methods.

The operation of the Laser Alignment System during the TIF slice test has shown that the laser beams operate properly. Useful laser signals were detected by all modules that were illuminated by the laser beams. In the worst-case scenario, where all observed laser spot shifts are assumed to come from structure deformations, the movements would be up to 600 μm. Assuming that most of the observed changes were coming from laser beam and alignment tube movements, shifts go down below 100 μm. To disentangle the two contributions and get a complete picture of the tracker deformations, more beams, distributed around all the 2π ϕ-range, have to be operated.

Finally, experience gained in alignment analysis of the silicon modules at the Tracker Integration Facility is valuable in preparation for the full CMS tracker alignment, which is crucial for high precision necessary to achieve the design physics goals of the CMS detector.

8 Acknowledgments

We thank the administrative staff at CERN and other Tracker Institutes. This work has been supported by: the Austrian Federal Ministry of Science and Research; the Belgium Fonds de la Recherche Scientifique and Fonds voor Wetenschappelijk Onderzoek; the Academy of Finland and Helsinki Institute of Physics; the Institut National de Physique Nucléaire et de Physique des Particules / CNRS, France; the Bundesministerium für Bildung und Forschung, Germany; the Istituto Nazionale di Fisica Nucleare, Italy; the Swiss Funding Agencies; the Science and Technology Facilities Council, UK; the US Department of Energy, and National Science Foundation. Individuals have received support from the Marie-Curie IEF program (European Union) and the A. P. Sloan Foundation.

References

[1] The CMS Tracker System Project TDR, CERN/LHCC 98-6, CMS TDR 5 (1998).
The CMS Tracker System Project TDR Addendum, CERN/LHCC 2000-016, CMS TDR 5 Addendum 1 (2000).

[2] CMS Collaboration, S. Chatrchyan *et al.*, "The CMS Experiment at the CERN LHC", 2008 JINST **3** S08004.

[3] W. Adam *et al.*, "Track Reconstruction with Cosmic Ray Data at the Tracker Integration Facility", CMS NOTE in preparation.

[4] W. Adam *et al.*, "Silicon Strip Tracker Detector Performance with Cosmic Ray Data at the Tracker Integration Facility", CMS NOTE 2008/032.

[5] P. Biallass, T. Hebbeker, "Improved Parameterization of the Cosmic Muon Flux for the Generator CMSCGEN", CMS NOTE 2007/033.

[6] M. Boezio *et al.*, "Energy spectra of atmospheric muons measured with the CAPRICE98 balloon experiment," Phys. Rev. D **67** (2003) 072003.

[7] V. Karimaki, T. Lampén, F.-P. Schilling, "The HIP Algorithm for Track Based Alignment and its Application to the CMS Pixel Detector," CMS NOTE-2006/018.

[8] E. Widl, R. Frühwirth, W. Adam, "A Kalman Filter for Track-based Alignment", CMS NOTE-2006/022.

[9] V. Blobel and C. Kleinwort, "A New Method for High-Precision Alignment of Track Detectors", contribution to the *Conference on Advanced Statistical Techniques in Particle Physics*, Durham, March 18-22 2002, `[hep-ex/0208021]`.

[10] V. Blobel, "Software Alignment for Tracking Detectors," Nucl. Instrum. Meth. A **566** (2006) 5.
A program description for Millepede II and the code is available via: `http://www.desy.de/~blobel`

[11] G. Flucke, P. Schleper, G. Steinbrück, M. Stoye, "A Study of Full Scale CMS Tracker Alignment using High Momentum Muons and Cosmics", CMS NOTE-2008/008.

[12] T. Lampén, N. de Filippis, F.-P. Schilling, A. Schmidt, M. Weber "Comprehensive Set of Misalignment Scenarios for the CMS Tracker", CMS NOTE-2008/029.